

Evaluation of Prone Breast PET/CT Imaging Using Phantoms

by

Songlin Sha

Duke Kunshan and Duke University  
Medical Physics Program

Date: \_\_\_\_\_

Approved:

\_\_\_\_\_  
Martin P. Tornai, Supervisor

\_\_\_\_\_  
Timothy G. Turkington

\_\_\_\_\_  
James E. Bowsher

Thesis submitted in partial fulfillment of  
the requirements for the degree of  
Master of Science in the Department of  
Duke Kunshan and Duke University  
Medical Physics Program in the Graduate School of  
Duke University

2019

ABSTRACT

Evaluation of Prone Breast PET/CT Imaging Using Phantoms

by

Songlin Sha

Duke Kunshan and Duke University  
Medical Physics Program

Date: \_\_\_\_\_

Approved:

\_\_\_\_\_  
Martin P. Tornai, Supervisor

\_\_\_\_\_  
Timothy G. Turkington

\_\_\_\_\_  
James E. Bowsher

An abstract of a thesis submitted in partial  
fulfillment of the requirements for the degree  
of Master of Science in the Department of  
Duke Kunshan and Duke University  
Medical Physics Program in the Graduate School of  
Duke University

2019

Copyright by  
Songlin Sha  
2019

## **Abstract**

The different patient orientations in breast PET/CT and breast MR imaging, supine versus prone, respectively, cause difficulty in integrating and interpreting the data acquired from these two types of imaging protocols. Prone breast PET/CT could be possible provided the assistance of a suitable support. The main purpose of this project is to evaluate the feasibility of prone breast PET/CT imaging using phantoms and to compare this protocol with the standard supine protocol from an image quality perspective. In this project, a rigid, weight-bearing, radiolucent foam support based on the dimensions and layout of the MRI breast coil for prone-pendant clinical breast imaging was devised for prone PET/CT imaging purposes. In order to scan the same test object in various configurations (prone versus supine), breast phantoms were investigated and tested to develop the most suitable combination of materials that can simulate breast morphology. Water-filled intravenous bags were determined to be the best choice for breast phantom development. The breasts containing lesions, along with a torso phantom, were scanned using a clinical PET/CT scanner in both prone and supine orientations. The acquired PET images were quantitatively evaluated in both orientations. Several image quality metrics such as signal-to-noise ratio, local contrast, contrast uniformity, and quantitative repeatability were assessed from the acquired PET data. As a result, prone PET images present better image quality than supine PET

images in terms of SNR and contrast uniformity. However, the uniformity of the signal intensity is worse in prone orientation, and there are several unexpected image artifacts. The paired t-test statistical results suggest that there are significant differences between prone and supine in terms of signal intensity and SNR. It can be concluded that prone PET/CT imaging is geometrically feasible with the assistance of the developed torso support. Prone PET/CT imaging holds advantages over supine PET/CT imaging considering registration with MRI.

# Contents

Abstract .....	iv
List of Tables.....	ix
List of Figures .....	xi
Acknowledgements .....	xiii
1. Introduction.....	1
1.1 Current status of breast imaging with PET .....	1
1.2 Breast phantom review .....	4
1.3 Purpose and Aims of this project .....	6
2. Materials and Methods.....	7
2.1 Torso support fabrication.....	7
2.2 Breast phantom material tests .....	11
2.2.1 Slime .....	12
2.2.2 Bolus material .....	15
2.2.3 Gelatin.....	16
2.2.4 Water .....	17
2.3 PET/CT imaging experiment .....	18
2.3.1 Lesion tree preparation.....	20
2.3.2 Malleable breast and torso phantoms preparation.....	21
2.3.3 PET/CT procedure specifications .....	24
2.4 Image Processing .....	26

2.4.1 Pixel replication and rescaling.....	26
2.4.2 VOI selection.....	27
2.5 Quantitative metrics.....	30
2.5.1 Average value.....	30
2.5.2 Standard Deviation.....	30
2.5.3 Signal-to-noise ratio.....	31
2.5.4 Local contrast.....	33
2.5.5 Contrast uniformity.....	34
2.5.6 Paired t-test.....	35
3. Results.....	36
3.1 Breast phantom material test results.....	36
3.2 Reconstruction and Imaging Analyses.....	37
3.2.1 General Analyses.....	38
3.2.2 PET image reconstruction with varying time intervals.....	39
3.2.3 PET image reconstruction with equal time intervals.....	41
3.2.4 Comparison Metrics—average signal and background.....	51
3.2.5 Comparison Metrics—SNR.....	53
3.2.6 Comparison Metrics—local contrast.....	54
3.2.7 Comparison Metrics—contrast uniformity.....	56
3.2.8 Comparison Metrics—paired t-test.....	56
4. Discussion.....	57
4.1 Caveats about the breast phantom materials.....	57

4.2 Factors that influence image quality in prone and supine PET images.....	58
4.3 Noise calculation in different situations.....	62
4.4 Resolution versus partial volume effect.....	63
4.5 Pros and cons of prone versus supine setup in PET/CT imaging.....	63
5. Conclusions.....	65
Appendix 1: BI-RADS Assessment Categories and Management Recommendations. ....	66
Appendix 2: Review—Breast Phantoms in Different Imaging Modalities.....	67
Appendix 3: Slime material tests. ....	69
Appendix 4: Gelatin material test.....	70
Appendix 5: Matrix of images (PET, prone, 420 sec reconstruction).....	71
Appendix 6: Matrix of images (PET, supine, 513 sec reconstruction) .....	73
Appendix 7: Matrix of images (CT, prone).....	75
Appendix 8: Matrix of images (CT, supine).....	77
Appendix 9: MRI experiment.....	79
References .....	83

## List of Tables

Table 1: Torso phantom and lesions specifications.....	20
Table 2: PET/CT scan parameters .....	26
Table 3: Breast phantom material test results. ....	37
Table 4: Average signal of 8 VOIs throughout equal time intervals (8 mm spheres, prone, units in $10^4$ Bq/mL).....	43
Table 5: Average background ( $\pm\text{STD}_{bkg}$ ) of 8 VOIs throughout equal time intervals (8 mm spheres, prone, units in $10^4$ Bq/mL) .....	44
Table 6: Average signal of 8 VOIs throughout equal time intervals (10 mm spheres, prone, units in $10^4$ Bq/mL) .....	45
Table 7: Average background ( $\pm\text{STD}_{bkg}$ ) of 8 VOIs throughout equal time intervals (10 mm spheres, prone, units in $10^4$ Bq/mL).....	46
Table 8: Average signal of 8 VOIs throughout equal time intervals (8 mm spheres, supine, units in $10^4$ Bq/mL).....	47
Table 9: Average background ( $\pm\text{STD}_{bkg}$ ) of 8 VOIs throughout equal time intervals (8 mm spheres, supine, units in $10^4$ Bq/mL) .....	48
Table 10: Average signal of 8 VOIs throughout equal time intervals (10 mm spheres, supine, units in $10^4$ Bq/mL).....	49
Table 11: Average background ( $\pm\text{STD}_{bkg}$ ) of 8 VOIs throughout equal time intervals (10 mm spheres, supine, units in $10^4$ Bq/mL) .....	50
Table 12: Average signal & background ( $\pm\text{STD}_{bkg}$ ) for each lesion sphere.....	53
Table 13: Average SNR ( $\overline{\text{SNR}}\pm\Delta\text{SNR}$ ) of each lesion sphere .....	54
Table 14: Average local contrast ( $\bar{C}\pm\Delta C$ ) of each lesion sphere.....	55
Table 15: Contrast uniformity .....	56
Table 16: Paired t-test (prone vs supine).....	56

Table 17: MR scan parameters..... 80

## List of Figures

Figure 1: Illustration of different patient setups.....	4
Figure 2: Photographs of the <i>Sentinelle</i> MR breast coil.....	8
Figure 3: Photographs of insulation foam materials used to fabricate the torso support..	8
Figure 4: Design sketch generated in <i>Solidworks</i> .....	9
Figure 5: Illustration of the assembly of foam pieces.....	11
Figure 6: Slime materials.....	14
Figure 7: Photograph of final cured bolus material. ....	15
Figure 8: Photographs of equipment and setup for the PET/CT experiment.....	19
Figure 9: Photograph of sealing the saline bags prior to the PET/CT scans. ....	22
Figure 10: Example of pixel scaling.....	27
Figure 11: Example of zoomed reconstructed (a) prone CT; (b) prone PET; (c) supine CT; (d) supine PET. ....	28
Figure 12: Profiles extracted from PET and CT matrices. ....	39
Figure 13: Prone PET images reconstructed over varying time intervals.....	40
Figure 14: Supine PET images reconstructed over varying time intervals.....	41
Figure 15: Average signal (solid curve) and background (dashed curve) for each lesion sphere (mean values over 10 measurements).. ....	52
Figure 16: Average signal-to-noise ratios of each lesion sphere. ....	54
Figure 17: Average local contrast of each lesion sphere.....	55
Figure 18: Diagram to illustrate the effect of pixel replication versus interpolation on calculating average. ....	59
Figure 19: Diagram of the locations of the spheres with respect to the image slices. ....	60

Figure 20: Example of artifacts in (a) CT image and (b) PET image caused by different factors.....	62
Figure 21: Phantom setup for the prone-only MR scan using the <i>Sentinelle</i> breast coil and <i>Siemens Skyra</i> scanner. ....	80
Figure 22: Matrix of images (MR, prone, STIR technique).....	81
Figure 23 (continued): Matrix of images (MR, prone, STIR technique) .....	82

## Acknowledgements

First, I would like to express my gratitude to my advisor Prof. Martin Tornai for the support of my research and the instruction on thesis writing. Besides, I would like to thank the rest of my thesis committee: Prof. Timothy Turkington and Prof. James Bowsher, who gave their detailed comments and hard questions.

My sincere thanks also give to Dr. Scott Robertson and Ms. Robin Davis, who helped a lot with my experiments. Many thanks to Dr. Ying-Chiang Huang, Dr. Fang-Fang Yin, Dr. Qiuwen Wu, Dr. Joshua Wilson, Ms. Maxi-Ann Campbell, Dr. Jing Cai, Dr. Wen Li, Dr. Xin Chen for their contributions to my coursework. Thanks to my lab mate Alan Register for working together with me and helping each other.

Last but not least, I would like to thank the faculty and students at both Duke and Duke Kunshan Universities, who gave their support throughout my graduate academic life.

# 1. Introduction

## 1.1 *Current status of breast imaging with PET*

Breast cancer is a tumor that develops from breast tissue. Symptoms of breast cancer include the appearance of lumps in the breast tissue, deformation of breast shape, and the emission of fluid from the nipple [1]. The diagnosis of breast cancer is highly reliant on different imaging techniques that take advantage of the differences in physical properties between cancerous and normal tissue, such as the transmission of acoustic waves, magnetic relaxation, X-ray attenuation, and *in vivo* detection of radioactivity to visualize the inner structure or the biological processes of the breast [2]. Depending on a patient's symptoms and the specific physician's requirements, the patient may need to undergo blood tests, mammography, breast magnetic resonance imaging (MRI), breast ultrasound (US), and breast positron emission tomography (PET)/ computed tomography (CT) in the diagnostic workup process [3]. These imaging techniques are very important in the diagnostic process of breast cancer because they help the physicians to determine the extent of the disease and the treatment method, which is called breast cancer staging. In terms of breast cancer staging, the breast imaging reporting and data system (BI-RADS), created by the American College of Radiology, is a widely accepted standard [3], and a complete list is attached in Appendix 1.

Traditional breast cancer screening techniques such as mammography and MRI can only provide anatomical information, which is insufficient for precise diagnosis and

these technologies have relatively low specificity. According to a study [4], up to 31% of all breast cancer cases may be over-diagnosed (high false positive rate) each year. Breast PET/CT imaging, however, can make up for this deficiency by providing both functional information (from PET) using appropriate radiotracers, and anatomical information (from CT). PET is a type of nuclear medicine imaging (NMI) technique. With this technique, the patient is injected with an appropriate radioactive pharmaceutical that circulates along the blood flow in the whole body. The thoracic region is then scanned to obtain images of the breast. The detectors of a PET scanner can capture 511-keV photons released by the annihilation of electrons with positrons emitted from a radionuclide (e.g.  $^{18}\text{F}$ ), and the collected lines of response help determine the interaction points in the reconstructed images. Thus, malignancies in the breast, which have a higher uptake of radiopharmaceutical than normal tissues do, appear as hot spots in a PET image. CT images of the same site are acquired immediately before/after the PET scan. Therefore, these two types of images can be registered with each other, fused, compared, and finally used to inform each other. There are various radiopharmaceuticals, such as  $^{18}\text{F}$ -fluorodeoxyglucose ( $^{18}\text{F}$ -FDG),  $^{18}\text{F}$ -alpha-methyltyrosine ( $^{18}\text{F}$ -MT),  $^{18}\text{F}$ -fluoroestradiol ( $^{18}\text{F}$ -FES), and  $^{11}\text{C}$ -methionine ( $^{11}\text{C}$ -Met), that can be used for breast PET imaging [5], and  $^{18}\text{F}$ -FDG is commonly used to evaluate the nearby lymph nodes and remote metastases.

The value of PET/CT in breast evaluation has been investigated extensively. The primary issues with most whole-body PET include its limited resolution and suboptimal

patient setup, which reduces the sensitivity for visualization of small tumors [6]. As there is an increased demand for accurate tumor visualization with PET in breast imaging, several studies have worked on dedicated PET systems for breast imaging. In 2009, MacDonald et al. evaluated a commercial positron emission mammography (PEM) system consisting of two planar detectors which have an improved resolution of 2.4 mm compared with the whole-body PET scanner [7]. Wu et al. presented a dedicated breast PET/CT system, in which patients were scanned in the prone position, with a single breast placed in the opening of the table [8]. A European project developed a mammograph with molecular imaging (MAMMI) PET system. In this study, the patient was also scanned in the prone position, with her breast hanging in a detector ring consisting of 12 detector modules [9]. This system had a resolution of less than 2 mm.

At the Duke Cancer Center, the common diagnostic process requires that the patient first takes a breast MRI to evaluate the stage of cancer, and then takes a breast PET/CT to check for metastases and to evaluate the nearby lymph nodes. The breast MRI is undertaken with the patient in a prone position, whereas a breast PET/CT scan is performed with the patient in a supine position (Figure 1). Although there are some achievable methods to realize MR-to-PET breast image registration providing the same prone patient setup [10], different patient setups make it challenging to spatially integrate and register the data obtained from MR and PET/CT. As the patient setup in breast MRI cannot be changed due to breast coil setup requirements, prone breast

PET/CT becomes a better starting point for further studies. It is noted that a prone breast PET scan would be feasible provided the assistance of a suitable supporting yet radiolucent structure beneath the patient, then it may be possible to change the current imaging protocol.



**Figure 1: Illustration of different patient setups. (a) Supine setup in breast PET scan. (b) Prone setup in breast MR scan. (The images are from the *Mayo Clinic* website.)**

## **1.2 Breast phantom review**

An imaging phantom is a specially designed object that is scanned in the field of view of the scanner to evaluate an imaging protocol or the performance of medical imaging devices. Depending on specific imaging purposes, phantoms can have different shapes to simulate the corresponding manner of human structure, and a breast phantom is one such example that aims to simulate the human breast. Various materials can be used to develop breast phantoms with different fabrication techniques. Due to the different physical principles of each imaging technique (e.g. MRI, US, X-ray, and NMI), special factors such as relaxation time, acoustic property, mechanical property, chemical

components, linear attenuation coefficient, and radiotracer half-life have to be considered when designing a breast phantom for a specific modality.

As the human breast is a soft organ that mainly consists of adipose tissue (~70%) and glandular tissue (~30%) [11], which have different appearance in anatomical images, there are anthropomorphic breast phantoms which can present the details of different breast tissues [12][13][14]. Since the shape of the breasts will change in different patient setups (supine or prone), the breast phantoms are capable of either fitting into the shape of compressed breasts or changing their shapes under different setups [15][16]. As water phantoms are commonly used in both MRI and NMI, some breast phantoms designed for these two modalities are fillable and reusable so that they can be filled with different liquids or materials for multiple purposes [17][18]. To evaluate the detectability of lesions in a breast with NMI, some fillable breast phantoms are inserted with specially designed inner structures to simulate lesions [18][19]. In terms of simulating specific breast tissues in the phantom, various substitute materials such as water [20][21][22], gelatin [23][24][25], agar [24][25][26], resin [13][14][15], lard [12][14], egg white [12][14], etc. are utilized to develop the breast phantom. Different fabrication techniques such as prototyping [13], inkjet printing [27], and 3D printing [14][19], can be used to make inner structures of the breast. There is a previous report by the author of this thesis that contains a comprehensive literature review on breast phantoms in different imaging modalities [28], and a summary list of the features, materials, fabrication techniques of

the breast phantoms used in different modalities is included in Appendix 2. Portions of that developmental work on breast phantom development are included in this thesis in Chapter 2.2.

### ***1.3 Purpose and Aims of this project***

The main purpose of this project is to evaluate prone breast PET/CT imaging and compare this protocol with the standard supine protocol from an image quality perspective using commonly known evaluation metrics. In order to achieve this objective, there are three specific Aims:

- i. Develop a prone support structure for breast PET/CT imaging that provides a setup similar to that for prone MRI.
- ii. Investigate and develop deformable breast phantoms suitable for comparing supine and prone patient orientations.
- iii. Use the torso support structure and deformable breast phantoms to investigate prone versus supine breast PET imaging.

## 2. Materials and Methods

In this section, materials and methods are discussed in detail, including the fabrication of a torso foam support used for prone breast PET imaging, breast phantom material tests, experimental procedures for PET/CT imaging, and details on image analysis.

### 2.1 Torso support fabrication

The eventual goal in developing this patient support is that its utilization in prone breast PET/CT imaging will enable patient setup that closely imitates that in MR imaging. Therefore, a torso support was devised based on the measured dimensions of the *Sentinelle* breast MR coil (*In vivo Corp.*) that is used at Duke Medical Center (Figure 2). The fabricated support was made of 5 cm thick insulation foam slabs (*Lowe's Home Improvement* product), which is an almost radiolucent material that should minimize the attenuation of 511 keV and X-ray photons but still retain a strong and rigid structure. It has a curved 30-degree slope with two D-shape cutouts on the flat top (where the patient's chest would rest), which is consistent with the breast MR coil. Four windows are left on both lateral sides for observation purposes. The length and width of the foam support are determined by the outer frame of the breast coil, and the D-shape cutouts roughly copy the geometry of the breast region in the coil. There is also a bottom extension at the front of the support to place the head support. Figure 3 shows the material and the general look of the final support.

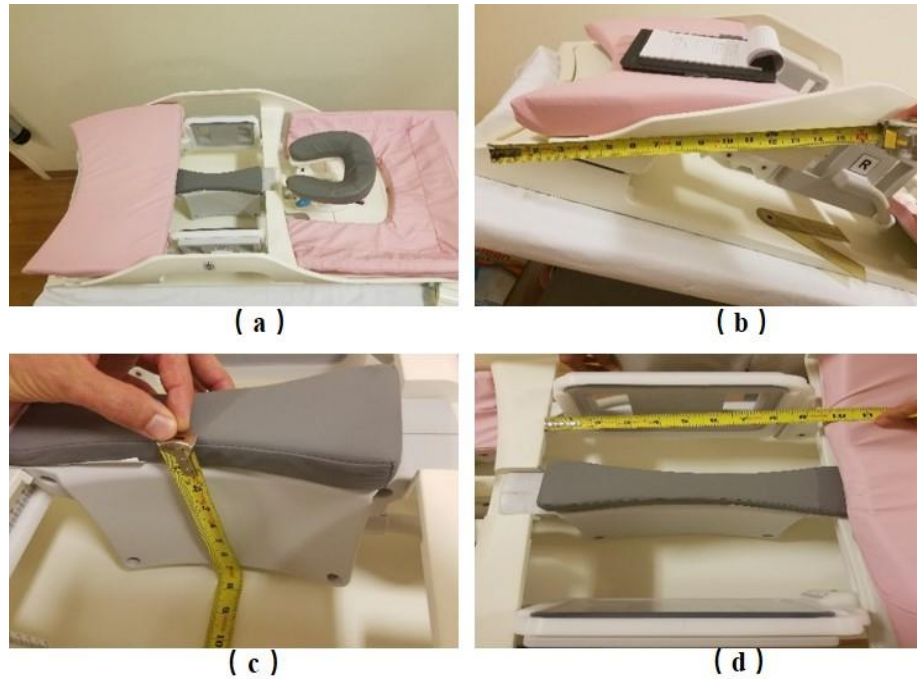


Figure 2: Photographs of the *Sentinelle* MR breast coil with a measurement ruler (in inches). (a) General look of the coil (creamy white structure) and paddings (pink and grey). (b) Slope of the coil where the patient's stomach will rest. (c) Height of the central coil that supports the mediastinum. (d) Geometry of the D-shaped breast openings that can also accommodate the MR biopsy apparatus.

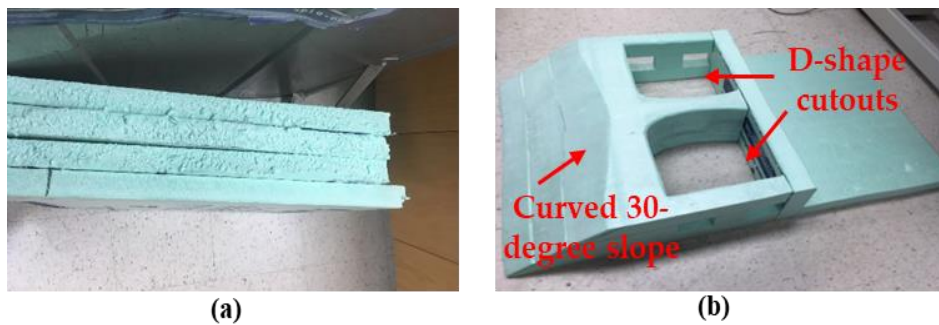
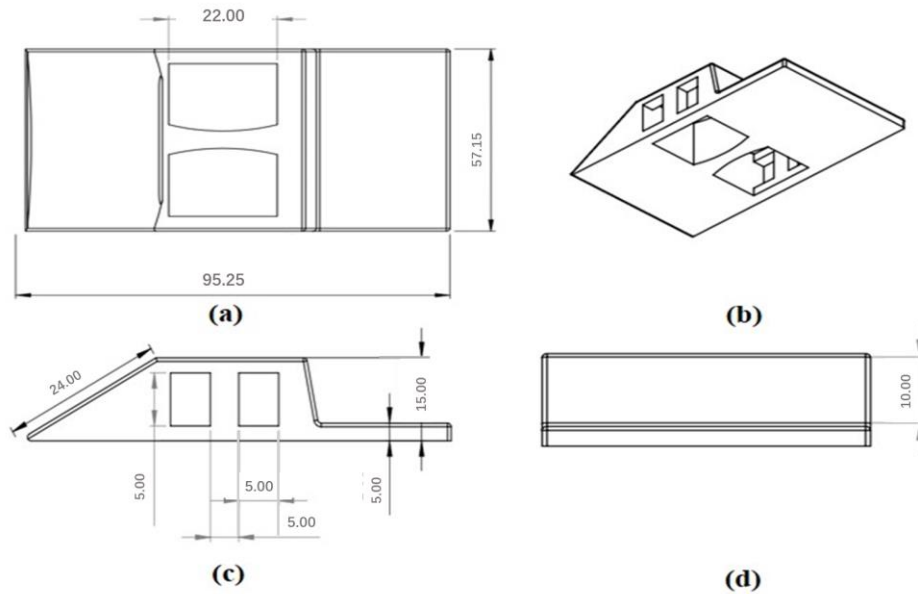


Figure 3: Photographs of insulation foam materials used to fabricate the torso support. (a) Stacked 5 cm thick foam slabs were glued together. (b) Final fabricated support.



**Figure 4: Design sketch generated in *Solidworks*. The unit of labeled numbers is centimeter. (a) Top-down view. (b) Overall anterior-lateral-oblique view (using torso habitus) from underneath the foam support. (c) Lateral view. (d) Front (or superior) view.**

Prior to fabrication, the torso support model was designed in *Solidworks* (Figure 4). Based on this detailed design sketch, the foam pieces were first roughly cut using a hand-saw, glued together, and then more finely cut using a bandsaw. These are the detailed steps:

- i. Cut three foam pieces into a rectangular shape with 60 cm length and 55 cm width, then bevel the short ends into 30-degree slopes. The leftover pieces can be used as a supporting piece when moving the foam slab along the bandsaw blade.

- ii. Stack the foam pieces from above with the sloped ends well aligned and temporarily tape them together as a whole, then vertically trim the other side to form a 50 cm long bottom piece.
- iii. Keep the foam pieces taped together, draw two symmetrical D-shape (22 cm length and 24 cm width) outlines on both top and bottom surfaces while sparing 3 cm wide lateral edges and leaving a 5 cm wide separation in the middle. In order to make these two symmetric cutouts, one of the cutouts has to be made by turning over the whole piece after the other is done.
- iv. Cut two more rectangular pieces that fit the width and the height of the whole piece to form the anterior cap and the bottom extension, then separate the middle piece and cut four windows of suitable sizes on both sides. Finely adjust or modify, if necessary, before gluing all the foam components together.
- v. Glue all the foam pieces together using *Elmers* all-purpose glue and rest lead weights on the foam stack. Insert bamboo sticks inside each joint to reinforce the strength of the support (Figure 5).
- vi. Make a curvature on the slope using a hand-file and sandpaper after the glue dries.

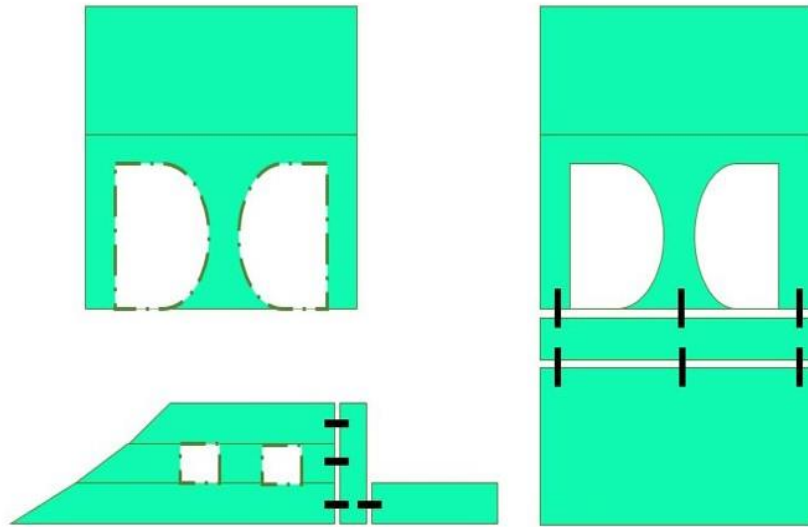


**Figure 5: Illustration of the assembly of foam pieces. The short bold lines represent bamboo sticks inserted in the foam for joint reinforcement.**

## ***2.2 Breast phantom material tests***

The aim of this experimental investigation is to find a malleable and flexible material for use as a breast phantom material for this imaging project. Since the imaging comparison to be made includes having the human subject lie prone or supine on a bed, the breast phantom (containing lesion spheres) should be able to re-conform itself from a supine to prone orientation by changing its shape. One selection criterion includes having volume conservation along with real-time moldability, such that the re-oriented breast phantoms containing objects of interest would simulate a real human breast under similar imaging conditions. Another criterion is that it should completely and uniformly contain the radioactivity (and any inserted lesion-like objects) distributed throughout its volume. Considering the relatively short half-life of  $^{18}\text{F}$  (109.7 min), the

time taken to form this breast-like material cannot be too long, and it should also be able to change its shape automatically to simulate the different morphologies of a breast in prone and supine positions. Four materials (manufactured “slime”, commercially available “bolus”, gelatin mix, and water or saline) were tested.

### **2.2.1 Slime**

“Slime” is a viscous, shapeable material made from commonly available *Elmer’s* glue and natural borax powder. After mixing these two substances together, sodium tetraborate, the effective chemical component in borax, can bond the polyvinyl acetate molecules in glue together to form a large polymer. The test on slime was performed using a controlled variable method, in which the volume of glue was kept constant while either the volume ratio of borax dissolved liquid to glue or the concentration of the borax solution was varied. The slime material was made and tested according to the following steps:

- i. Dissolve enough borax powder in a suitable amount of tap water (~300 mL) in a measuring beaker at room temperature (~23 °C) and stir the solution until the powder remaining on the bottom cannot be further dissolved. Borax is hard to dissolve in water, and it has a solubility of approximately 6 g/L under room temperature.
- ii. Separate the upper saturated borax solution into three equal portions in measuring beakers to prepare three different concentrations of borax

solution. The first solution was diluted to half the saturated concentration under room temperature by adding tap water until the current volume of the solution is doubled, thus its concentration was approximately 3 g/L. The second solution (with some undissolved borax powder) was put into the microwave and heated for 3 minutes (~50 °C) to dissolve more of the undissolved borax. This resulted in an increased concentration of approximately 10 g/L. The last solution was the saturated borax solution under room temperature (~23 °C) which had a concentration of approximately 6 g/L.

- iii. Pour suitable amounts of *Elmers* all-purpose glue (~50 mL) in a measuring beaker and add in different concentrations of borax solution (3 g/L, 6 g/L, 10 g/L) by different volume ratios ( $V_{\text{glue}}:V_{\text{borax}} = 1:1, 1:2, 2:1$ ).
- iv. In order to visualize the effect of mixing the breast slime with an added radiopharmaceutical, some pigment was added into the glue or borax solution before mixing the two compounds to simulate the radioactivity in PET procedure.
- v. Stir and squeeze the blended materials until the slime material looks uniform. Repeat steps iii-v, and six different tests were made.

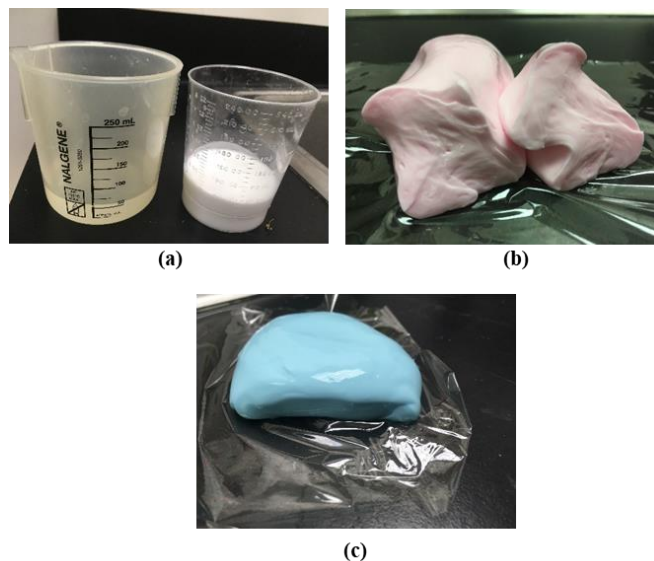


**Figure 6: Slime materials. (a) Water and glue needed to make the material. (b) Sliced section of slime material with red pigment added and literally folded into the hardening borax solution. (c) Slime material with blue color added into the glue.**

A complete experiment list of slime material is attached in Appendix 3. Figure 6 shows the final slime materials. It was determined that increasing the volume ratio of borax solution to glue, or lowering the concentration of borax solution did not change the final consistency of the slime material. However, the material failed to form when the initial volume of the borax solution was less than the volume of glue. Even given more borax solution, the glue would only absorb an amount of borax solution corresponded to 60% of its own volume. Thus, in order to avoid the overuse of materials, the best way to make slime material is to mix the glue with borax solution with equal volumes. A higher concentration of borax solution would decrease the time of formation, but this resulted in a harder and less stretchy material. Although the slime material can be formed relatively quickly (less than 10 min) and has a uniform coloring

distribution after considerable mixing and folding, it is not a suitable material for breast phantoms for this project because it has slow mobility and is optically opaque. In other words, this material does not change its shape easily automatically, but rather requires external forces. As such, it cannot simulate the morphology of breasts in different setups. Furthermore, the locations of inserted objects of interest, such as lesions, cannot be visualized due to the optical opacity.

### **2.2.2 Bolus material**

Bolus, normally used in radiation therapy, is a commercial material that can simulate human tissue [29]. It has a density of  $1.02 \text{ g/cm}^3$  and is highly malleable [29]. A pack of 30 g sample powder (*Super Stuff Bolus, Radiation Products Design Inc., Albertville, MN, USA*) was tested for this project. The bolus material was made by adding about 200 mL tap water into the powder bag and kneading the bag until the lumps in the material disappeared. It had to sit overnight before a uniform consistency of bolus material can be achieved.



**Figure 7: Photograph of final cured bolus material. No colorant was added.**

Figure 7 shows the final congealed bolus material. The time taken for bolus material formation was about 12 hours, which is much longer than the half-life of  $^{18}\text{F}$  (109.7 min) used in PET procedures. This is problematic since radioactivity would largely decay away before full bolus formation. Once the material was formed, pigment could no longer be absorbed or diffused into the finished material, even if the material was kneaded. Although the bolus material has more mobility than the slime and also has similar characteristics to breast tissue, it is not a suitable material for the development of breast phantoms in this project due to the long time-of-formation. Its opacity also inhibits the visualization of any internal objects.

### **2.2.3 Gelatin**

Gelatin is an easily accessible material with a viscous texture and has been used for breast phantom fabrication in several studies [16][19][25]. Gelatin powder has low solubility but can be dissolved in hot water. Since it turns from the liquid phase to the solid phase during formation, it can be molded into different shapes. Gelatin was feasible for PET procedures in some cases [16][19], and its mechanical and acoustic properties were evaluated for ultrasound breast imaging purpose [25], so its suitability for the purpose of this project was investigated. Gelatin was made according to the following steps:

- i. Weigh out 2 g, 5 g, 10 g gelatin powder using an electronic scale.

- ii. Heat up 600 mL water in the microwave oven for 5 minutes (~70 °C) and separate it into 3 measuring beakers with 200 mL in each.
- iii. Add the gelatin powder into hot water and keep stirring it until the powder is totally dissolved. Thus, three beakers of liquid roughly contain 1%, 2.5%, and 5% of gelatin by weight.
- iv. Wait until the liquid cools off and solidifies (standard refrigeration speeds up this process).

The time taken for the final gelatin materials to be formed was more than an hour. The stiffness of the final materials increased with the amount of gelatin powder. The final material made with 1% gelatin failed to solidify because insufficient gelatin was used; rather, the liquid merely had more solute than plain water but otherwise behaved like water. Although gelatin has a viscous or jellied texture which is close to human tissue, and it is optically clear, its shape cannot change automatically once it is molded. Therefore, gelatin is not considered a suitable material to form a breast phantom in the context of this project.

#### **2.2.4 Water**

As none of the tested materials proved suitable for developing breast phantoms that met the requirement of this project, saline-filled intravenous bags were tested. This idea credits Williams et al.'s work [30], in which two pendant saline bags were attached to the anterior surface of a torso phantom to simulate the manner of breast orientation in

supine or prone positions in a PET/CT scanner. Different volumes of intravenous bags were tested for this project (see in section **2.3.2 Malleable breast and torso phantoms preparation**), and a 1 L bag with 250 mL liquid removed was decided to be the best for use. The remaining 750 mL of water can just simulate the average volume of a female breast [31]. The water bag became fairly flexible and mirrored the characteristics of the breast quite closely if the air was totally evacuated from it, and there was still room for the fluid to flow throughout the bag.

We used a modified version of the water bags containing less fluid than the 1 L bag volume, and also containing a string of spherical lesions with a fixed lesion-to-background radioactivity concentration ratio. Detailed descriptions of the utilized breast phantoms are described in the next section.

### **2.3 PET/CT imaging experiment**

In Williams' earlier work [30], their objective was to determine differences in Standardized Uptake Value (SUV) between supine and prone breast orientations and investigate how these differences might impact clinical breast imaging quantification. In the present thesis research, we were interested in signal (e.g. lesion) characteristics within and throughout a breast, with lesions located at various locations throughout the breast volume.

In this project, we used a fillable anthropomorphic torso phantom (model ECT/TOR/P, *Data Spectrum Corp.*, Durham, NC, USA) in which there are two shaped

inserts containing Styrofoam beads to simulate the lungs, a Teflon rod to simulate the spinal cord, and a shaped compartment to simulate the liver (Figure 8). A complete list of specifications of the torso phantom is listed in Table 1. A novel aspect of this project is that two flexible lesion trees were developed, then inserted into each of the breast phantoms to evaluate the effect of different setups on lesion signal detection. The phantoms were prepared as described in the following sections. Both prone and supine PET/CT images were acquired using the *GE Discovery-IQ* PET/CT scanner (*General Electric Healthcare, Waukesha, WI*), first with prone experiments utilizing the developed foam support (Figure 3).

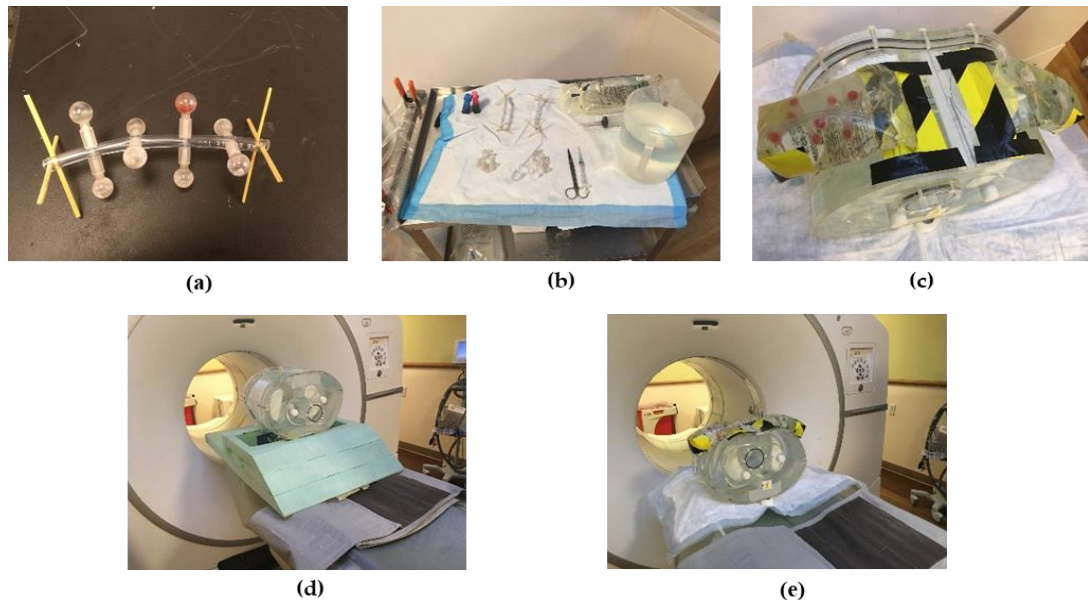


**Figure 8: Photographs of equipment and setup for the PET/CT experiment. (a) Geometry of the lesion tree. (b) Tools needed for the experiment. (c) Finished phantom in supine orientation with breasts attached near the torso phantom mediastinum. (d) Prone phantom setup supported by the foam patient support on the PET/CT bed. (e) Supine phantom setup without the need for the foam support.**

**Table 1: Torso phantom and lesions specifications.**

<b>Torso Phantom Dimensions</b>	<b>Outer widths</b>	26 cm anterior-posterior × 38 cm lateral
	<b>Inner widths</b>	24 cm anterior-posterior × 36 cm lateral
	<b>Wall thickness</b>	9.5 mm
<b>Torso Phantom Volumes</b>	<b>Left lung (with foam beads)</b>	~0.36 L
	<b>Right lung (with foam beads)</b>	~0.44 L
	<b>Liver</b>	~1.2 L
	<b>Torso</b>	~9.77 L
<b>Lesion Dimensions</b>	<b>Inner diameters</b>	8 mm / 10 mm
<b>Lesion Volumes</b>	<b>Inner volumes</b>	0.268 mL / 0.564 mL

### 2.3.1 Lesion tree preparation

Instead of using a uniform breast phantom as in Williams' earlier work [30], this study utilized fillable spheres providing realistic lesion-like signals. Lesions of different sizes and locations throughout the breast volume were utilized on a flexible and controllable mounting fixture for imaging with PET and CT imaging.

A single 12.5 cm soft plastic tube (*Lancer Lab Bubble Tubing 8889-224203*) was equipped with four orthogonally oriented and equally spaced nylon plastic screw-rods, upon which four pairs of identically sized acrylic plastic spheres were fixed. The benefit of this design is that the soft plastic tube provides a uniform, symmetrical and defined lesion distribution throughout the breast in different orientations, while it maintains some flexibility for the lesion spheres to twist or move under different breast

configurations. On either end of the tube were two pairs of vertically crossed bamboo sticks, whose length was a little longer than that of a lesion pair; these crossed bamboo spacers were intended to push up the surface of the saline bags and prevent the spheres from getting too close to the breast surface or the chest wall given different orientations of the breast. The lesions were provided by Dr. Turkington's laboratory and were loosely modeled on spherical lesions from *Data Spectrum Corp.* (model ECT/ HOL-468/A, Durham, NC, USA). The completed lesion tree is shown in Figure 8-a (in air) and 8-c (within the breasts). Two lesion trees were prepared for this experiment, and the two attached sets of 8 lesion spheres were 8 mm and 10 mm inner diameter within each breast, corresponding to 0.268 mL and 0.524 mL volumes, respectively.

### **2.3.2 Malleable breast and torso phantoms preparation**

Since the purpose of the measurements is to determine any differences between the prone and supine orientations, the breast phantom needs to have certain characteristics. It needs to: have constant volume; be large enough to support the insertable lesions of interest; be flexible such that it can transform in shape from the prone to supine orientations; be water-tight so that it can safely contain the radioactive fluid; be easy to use. Upon initial investigation, 500 mL and 1 L isotonic saline bags (*Baxter Healthcare Corp*, Deerfield, IL, USA) were identified; given that the average breast size of patients scanned with MRI at Duke was measured to be 740 mL [31], we chose to use the larger 1 L saline bag, which also allowed draining of fluid, leaving the bag partly

full. Several experiments to seal the bags containing the lesions were undertaken, and the utilized method is described in the next paragraph (Figure 9).

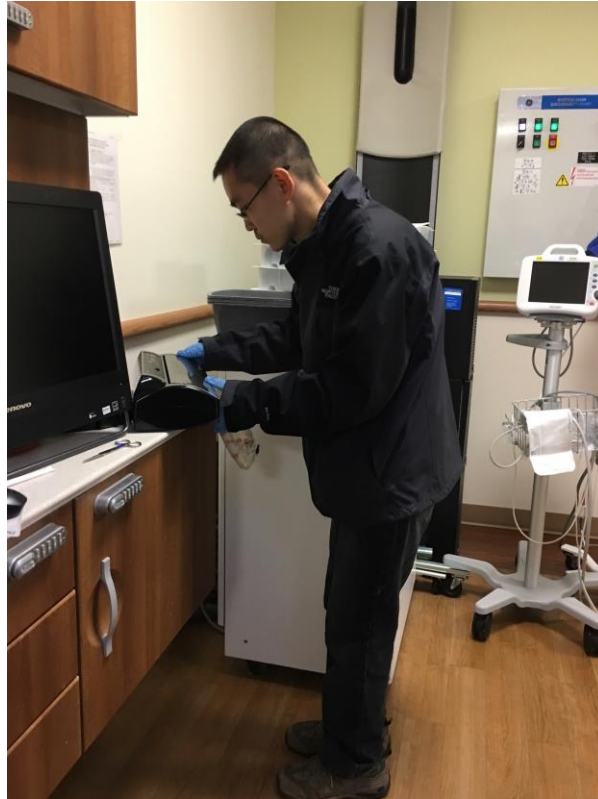


**Figure 9: Photograph of sealing the saline bags prior to the PET/CT scans.**

Two 1 L saline bags, one for each breast, were used in this project and were prepared the same way. The flat end of the saline bag (where the notch is located to hang the bag) was first cut off to empty out the liquid and allow insertion of the prepared (radioactivity containing) lesion tree. The bag was then resealed 3 times for 5 sec sealing times each, using a commercially available heated bag sealer (Foodsaver, *Sunbeam Products, Inc.*, Boca Raton, FL, USA). Tape was attached to the seams to avoid leakage and retain the bag in an approximate breast shape. After resealing the bag

containing the lesion tree, 750 mL of saline (with radioactivity) was refilled into the bag through the tube end. Air was evacuated to allow mobility of the breast fluid within the confined volume without sloshing around in a space with an air bubble. Upon completion of these steps, the bags were taped onto the medial anterior surface of the torso phantom for scanning. Figure 8-c shows the finished breast and torso phantoms. The two lesion trees were distinguished by different coloring: blue ones are 8-mm diameter spheres, and red ones are 10-mm diameter spheres.

The torso phantom has a fillable volume of 9770 mL, corresponding to an approximate volume of 10 L (model ECT/TOR/P, *Data Spectrum Corp.*, Durham, NC, USA). The shell is able to contain 12 L of water if the lungs and spinal cord are removed, making the torso suitable as a mixing vessel as well. The total utilized <sup>18</sup>F<sup>18</sup>FDG activity was 4.05 mCi (including lesions). The workflow for PET/CT preparations is as follows:

- i. Empty 1.5 L of saline from the two saline bags into a measuring beaker for use.
- ii. Inject all the <sup>18</sup>F<sup>18</sup>FDG into the measuring beaker, mix well, and take out approximately 10 mL of radioactive saline for filling all the lesions. Separate the extracted 10 mL saline into two equal portions and add blue and red pigments for each of the 8 mm and 10 mm lesion diameters, respectively.
- iii. Fill the torso with 10 L of water and add the 1.5 L of radioactive saline, mixing it to get homogeneity. Extract 1.5 L of the diluted radioactive water

from the torso phantom to use to fill the saline bags (750 mL each). Thus, the torso phantom will contain ~10 L of radioactive water. The benefit of this procedure is that the torso and the breasts will have the same uniform radioactivity concentration and distribution for background, and the activity concentration in the lesions will be approximately 8X greater. From 1.5 L to 11.5 L, the volume increases by a factor of 7.7, which means the activity concentration in the lesion spheres is roughly 7.7 times that of the background.

- iv. After the breast phantoms are prepared and attached to the torso phantom following the methods described earlier, the whole phantom is ready to be scanned.

### **2.3.3 PET/CT procedure specifications**

The phantom was first placed anterior-side down on the foam support in a “head in/foot out” orientation to perform a prone scan (Figure 8-d). Each breast was gently suspended inside the openings of the foam support (Figure 3-b, Figure 8-d).

The phantom was scanned using the *GE Discovery-IQ* PET/CT scanner. A complete list of parameter settings for the PET/CT experiment is shown in Table 2. First, we had to determine the vertical clearance, and axial scan range of the phantom within the 70 cm diameter PET/CT gantry. Thereafter, the phantom underwent a CT scan, a 2-minute short PET scan, and a 15-minute long PET scan in time sequence. Then, the foam

support was removed from the bed and the phantom was changed to the supine setup (Figure 8-e). Scans taken with this setup included a CT scan, a 2-minute short PET scan, and a 20-minute long PET scan. List files were recorded to allow subsequent replaying of counts into dynamic sinograms. Using *GE's VUE-Point HD* (VPHD) software (matrix size 128×128, FOV 50 cm), the PET images were reconstructed using an ordered subsets expectation maximization (OSEM) algorithm (12 subsets, 4 iterations, 6.4 mm Gaussian filter smoothing) with scatter, attenuation, and randoms corrections applied. The 15 min prone acquisition was replayed into frames of 8, 15, 30, 60, 120, 240, and 420 seconds. It was also replayed into ten 90-s frames. In other words, 10 independent measurements are reconstructed (i.e. replayed) so that the ensemble averages of the various calculated metrics could be determined; this will be discussed in detail in section 2.6. Similarly, the 20 min supine acquisition was replayed into frames of 9, 18, 37, 73, 146, 292, and 513 seconds. It was also replayed into 10 frames with 110-s each. The supine time frame case is relatively longer than the prone case in order to compensate for the radioactive decay of  $^{18}\text{F}$  from the earlier prone acquisitions.

**Table 2: PET/CT scan parameters**

Experiments (in chronological order)		Time duration	FOV ( $cm^2$ )	Scan range (cm)	Slice thickness (mm)	Number of slices	Pixel size ( $mm^2$ )
Prone	CT scan	~20 s	50 × 50	26	3.26	79	0.9766 × 0.9766
	short PET scan	2 min					3.9 × 3.9
	long PET scan	15 min					
Supine	CT scan	~20 s	50 × 50	26	3.26	79	0.9766 × 0.9766
	short PET scan	2 min					3.9 × 3.9
	long PET scan	20 min					

## **2.4 Image Processing**

### **2.4.1 Pixel replication and rescaling**

The reconstructed PET images have a matrix size of 128×128, whereas the matrix size of CT images is 512×512. For calculation purposes, the PET image is resized to a larger matrix in *Matlab* by replicating a single coarse pixel to 16 smaller sized pixels (in a 4×4 matrix) assigned with the same pixel value. Thus, both PET and CT image matrices will have the same size (512×512) and pixel width (0.98 mm) and will be sampled in the same way. However, the finer sampled PET image cannot compensate for its limited spatial resolution because its content may not be well aligned with the corresponding CT image. Another method of resampling is to convert both two types of images to a matrix of 256×256 by up-sampling the PET image by a factor of 2 meanwhile down-

sampling the CT image by a factor of 2, which is also a reasonable method but has not been proved to be the correct method<sup>1</sup>.

For display purposes, the DICOM PET images are scaled to the same window level by default (each image has its own scaling factor), leading to different global values in the regions of interest (ROIs) in different slices. Therefore, for each slice, the pixel values must be multiplied by that slice's scaling factor to retrieve their original pixel values for calculation purposes. As an example, Figure 10 shows the means of the same ROI in three different slices before and after pixel scaling.

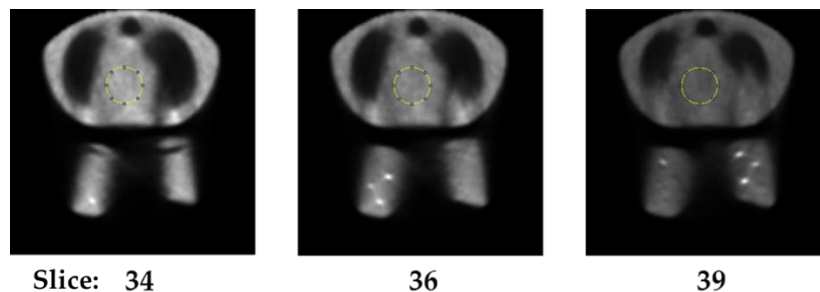


**Figure 10: Example of pixel scaling. The means of the same yellow circular ROI in slice 34, 36, and 39 before pixel scaling are 20952, 16616, and 10779 yielding a standard deviation of 5104. After pixel scaling, those means become 7571, 7584, and 7632 with a standard deviation of 32.**

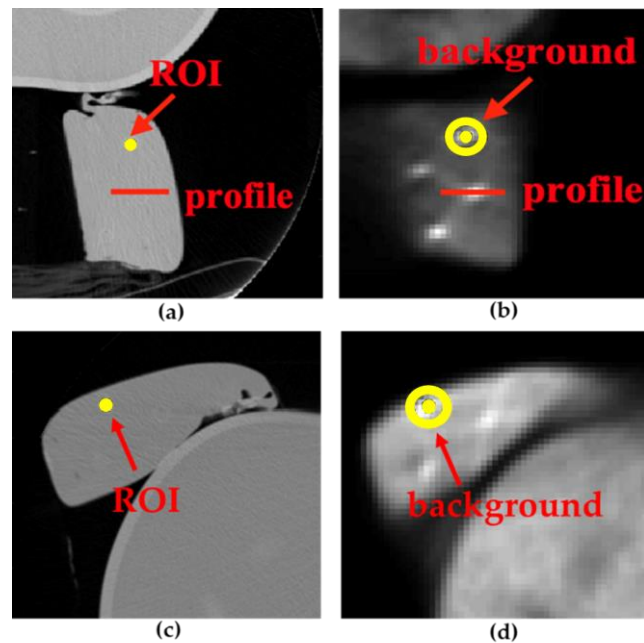
## 2.4.2 VOI selection

Figure 11 shows an example of zoomed and cropped CT and PET images in the prone and supine setups. The x-y coordinates of the center of the lesions, as well as the CT slices on which these lesions appear, were manually determined by visually

---

<sup>1</sup> Unpublished, personal communication from Dr. Turkington.

inspecting the CT images. These coordinates and slice numbers then served as inputs for a *Matlab* script that creates circular regions of interest (ROI) on the corresponding PET image slices. The center of each lesion had the same x-y coordinate on each PET slice. This circular ROI is shown as a yellow circle in Figure 11. The circular ROI has a diameter slightly smaller than the real diameter of the sphere. An annular region around the lesion was also obtained from the PET image as the local background and is shown as a yellow ring in Figure 11. It shares the same center with the lesion-ROI, and its inner and outer diameters are, respectively, 2 and 3 times larger than the sphere's actual diameter.



**Figure 11: Example of zoomed reconstructed (a) prone CT; (b) prone PET; (c) supine CT; (d) supine PET. The yellow circular and annular regions are the lesion and background ROIs used to obtain data from the PET image for calculation. The red horizontal lines represent example profile locations taken from both CT and PET images.**

Generally, spherical lesions with 8 mm inner diameters (0.268 mL in volume) can be visualized in up to 3 adjacent slices, and those with 10 mm inner diameters (0.524 mL in volume) can be visualized in up to 4 adjacent slices. Thus, for both breasts of the torso phantom, each lesion has independent consecutive 3 or 4 PET image slices. The location of each lesion is distinct in each PET image, and the center of the lesion can be determined by comparing both PET and CT images of the same slice. To determine the volume of interest (VOI) for each lesion sphere, circular ROIs were extracted from each PET image series in each lesion area, and their diameters were scaled down by a factor of 0.67, 0.9, 0.67 for 8-mm spheres and 0.4, 0.9, 0.9, 0.4 for 10-mm spheres with respect to the actual diameter of the lesion. For each lesion, its VOI was determined by the sum of the lesions' corresponding consecutive ROIs. For example, 87 and 164 total pixel elements were taken out to make up the VOIs for 8 mm-spheres and 10 mm-spheres, respectively. Given that the size of a single voxel in both PET and CT images is  $0.98 \times 0.98 \times 3.26 \text{ mm}^3$ , the volumes of the extracted VOIs were  $0.98 \times 0.98 \times 3.26 \times 87 \approx 0.27 \text{ mL}$  and  $0.98 \times 0.98 \times 3.26 \times 164 \approx 0.51 \text{ mL}$  respectively, which are in agreement with the real volumes of the spheres.

Similarly, annular VOIs (804 elements for 8 mm-sphere background and 1664 elements for 10 mm-sphere background) were obtained around the lesion for local background calculation. A problem of the background in supine PET images is that the locations of some lesions were very close to the surface of the saline bag, and some

regions outside the breast (i.e. air, located around the prone-pendant and anterior to the supine breast, and plastic, located at the posterior breast in both prone and supine orientations) may be included in the background area. Therefore, for the backgrounds obtained from supine PET images, those elements whose values are less than 400 (considering the scaling factor) were assumed to be outside the breast and were masked out from the local background ROI determination.

## **2.5 Quantitative metrics**

### **2.5.1 Average value**

In PET imaging, particularly, a voxel in the quantitatively reconstructed PET image has units of integrated radioactivity concentration. Therefore, the average estimated activity concentration is determined by the following formula:

$$\bar{A} = \frac{1}{m} \sum_{i=1}^m n_i \quad (i \in \text{VOI}), \quad \text{Eqn. 2.1}$$

where  $\bar{A}$  is the average estimated activity concentration of a VOI,  $m$  is the total number of voxels in the VOI,  $n_i$  represents the rescaled value of a single voxel  $i$  in the VOI. Note that the VOI applies either to a lesion or to a region of the background. In a broader sense, the average value can also be interpreted as signal intensity, which will be mentioned in section 2.6.3.

### **2.5.2 Standard Deviation**

The standard deviation (STD) of the background reflects the variation of the signal intensity relative to its mean value in the background VOI and is often used as

surrogate for image noise when the pixel values are uncorrelated. In this thesis, it will be referred to as the STD. It is calculated according to the formula:

$$\text{STD}_{bkg} = \sqrt{\frac{1}{m-1} \sum_{i=1}^m (n_i - \bar{n})^2} \quad (i \in BKG), \quad \text{Eqn. 2.2}$$

where  $\text{STD}_{bkg}$  denotes the standard deviation of the background,  $m$  is the total number of voxels in the background VOI,  $n_i$  represents the rescaled value of a single voxel  $i$  in the background VOI, and  $\bar{n}$  is the mean value calculated from the voxels in the background VOI. This method calculates the pixel-by-pixel variation in the background, which includes both random effects (fluctuation in the number of photons) as well as non-uniformity (e.g. streaks, other artifacts, etc.) in the reconstructed images.

The standard deviation formula can also be applied to a specific metric acquired from various independent measurements (Eqn. 2.5, Eqn. 2.9). In this case, the standard deviation evaluates the statistical fluctuation and the repeatability of the measurements for this metric, relative to its mean value.

### 2.5.3 Signal-to-noise ratio

Signal-to-noise ratio (SNR) is a metric that reflects the detectability of an object distinguished from the background noise, and it refers to the signal intensity relative to the ambient noise. Given the average of the VOI and the standard deviation of the background, the SNR of a single sphere can be calculated by:

$$SNR = \frac{\overline{S_{VOI}} - \overline{S_{bkg}}}{STD_{bkg}}, \quad \text{Eqn. 2.3}$$

where  $\overline{S_{VOI}}$  and  $\overline{S_{bkg}}$  are the average signals in the lesion and background VOIs obtained using Eqn. 2.1, and  $STD_{bkg}$  is the standard deviation of the background obtained using Eqn. 2.2. The numerator gives the relative difference of the signals between the lesion and background VOIs, which is considered to be the amplitude of the signal, and the standard deviation of the background is surrogate for the amplitude of noise in the definition of SNR.

The SNR of a single sphere can be determined for each measurement. Thus, the average SNR (denoted as  $\overline{SNR}$ ) across N measurements can be calculated by:

$$\overline{SNR} = \frac{1}{N} \sum_{i=1}^N SNR_i, \quad \text{Eqn. 2.4}$$

and the standard deviation of the SNR (denoted as  $\Delta SNR$ ) across N measurements can be calculated by:

$$\Delta SNR = \sqrt{\frac{1}{N-1} \sum_{i=1}^N (SNR_i - \overline{SNR})^2}. \quad \text{Eqn. 2.5}$$

$\Delta SNR$  calculates the statistical fluctuation of the measured SNR relative to the mean value, which reflects the reliability of the SNR measurements. Furthermore,  $\Delta SNR$  can be used to estimate the standard error of the SNR across N measurements [denoted as  $\sigma(\overline{SNR})$ ], which is determined by the propagation of error equation:

$$\sigma(\overline{SNR}) = \sqrt{\sum_{i=1}^N \left( \frac{\partial \overline{SNR}}{\partial SNR_i} \cdot \Delta SNR_i \right)^2} = \frac{\Delta SNR}{\sqrt{N}}. \quad \text{Eqn. 2.6}$$

From Eqn. 2.4 to Eqn. 2.6,  $SNR_i$  represents the SNR calculated for each measurement  $i$ , and  $N$  represents 10 measurements in the cases of this study.

#### 2.5.4 Local contrast

Local contrast is a metric that reflects the conspicuity of an object, in other words, how well it can be seen by a typical observer. Local contrast refers to the difference of the signal intensity between an object and its surrounding background. It is given by the relative difference between the average VOI and the average background divided by the average background and is calculated by:

$$C_L = \frac{\overline{S_{VOI}} - \overline{S_{bkg}}}{\overline{S_{bkg}}}. \quad \text{Eqn. 2.7}$$

Here,  $C_L$  denotes local contrast,  $\overline{S_{VOI}}$  and  $\overline{S_{bkg}}$  represent the average signals of VOI and background, respectively.

Similar to the SNR calculations, the average contrast (denoted as  $\bar{C}$ ) across  $N$  measurements can be calculated by:

$$\bar{C} = \frac{1}{N} \sum_{i=1}^N C_i, \quad \text{Eqn. 2.8}$$

and the standard deviation of the contrast across  $N$  measurements (denoted as  $\Delta C$ ) is calculated by:

$$\Delta C = \sqrt{\frac{1}{N-1} \sum_{i=1}^N (C_i - \bar{C})^2}. \quad \text{Eqn. 2.9}$$

$\Delta C$  calculates the statistical fluctuation of the measured local contrast relative to its mean value, which reflects the reliability of the contrast measurements. Furthermore,  $\Delta C$  can be used to estimate the standard error of the local contrast across  $N$  measurements [denoted as  $\sigma(\bar{C})$ ], which is determined by the propagation of error equation:

$$\sigma(\bar{C}) = \sqrt{\sum_{i=1}^N \left( \frac{\partial \bar{C}}{\partial C_i} \cdot \Delta C_i \right)^2} = \frac{\Delta C}{\sqrt{N}}. \quad \text{Eqn. 2.10}$$

From Eqn. 2.8 to Eqn. 2.10,  $C_i$  represents the calculated local contrast for each measurement  $i$ , and  $N$  also represents 10 measurements in the cases of this study.

### 2.5.5 Contrast uniformity

Contrast uniformity is a metric to evaluate the contrast throughout the breast.

For each measurement, the standard deviation of the contrast across all the lesions (denoted as  $\Delta C_i$ ) is calculated by:

$$\Delta C_i = \sqrt{\frac{1}{M-1} \sum_{j=1}^M (C_{i,j} - \bar{C})^2}, \quad \text{Eqn. 2.11}$$

where  $C_{i,j}$  represents the calculated contrast for a single lesion  $j$  in measurement  $i$ , and  $M$  represents 8 lesions. Thus, contrast uniformity is determined by averaging the standard deviation of the contrast over the lesions across  $N$  measurements:

$$CU = \frac{1}{N} \sum_{i=1}^N \Delta C_i, \quad \text{Eqn. 2.12}$$

where CU represents contrast uniformity,  $\Delta C_i$  is the standard deviation of the contrast across all the lesions for each measurement  $i$  obtained from Eqn. 2.12, and N represents 10 measurements in the case of this study.

### **2.5.6 Paired t-test**

To quantify the effect of prone versus supine positioning on the calculated metrics, a paired t-test was performed on the acquired average signal intensity, SNR, and local contrast. The aim of paired t-test is to compare two population means of two different methods of measurement (prone vs supine) on the same objects (8-mm or 10-mm spheres) [33]. The paired t-test is quantified by p-value, which is the probability that the difference of the compared results occurred by chance. The null hypothesis is that different setups have no effect on the image quality.

## 3. Results

### 3.1 *Breast phantom material test results*

A comprehensive evaluation of four breast phantom materials tested for this project is listed in Table 3. The materials are rated from 1 to 10 in terms of how easy it is to shape it (malleability) and how easy it is to lose its shape (mobility). To some extent, all of the three materials (excluding water) are malleable. However, their other properties (e.g. opacity) made the materials unsuitable for the purposes of this project. As radioactivity (usually in the form of a liquid) is necessary for PET procedures, the choice of breast phantom materials requires the consideration of the relatively short half-life of the isotope ( $^{18}\text{F}$ , or potentially shorter-lived isotopes as well) since the breast phantoms have to be made on-site. Although, bolus material presented promising malleability characteristics, its time of formation was too long for our purposes. Slime and gelatin could be used for PET procedures, but once they are less malleable, they are fixed in whatever formed shape and cannot change their shape easily.

Water proved to be the optimal material to make the breast phantoms for this project for several reasons. First, water-filled saline bags can not only simulate the breast morphology, but also their flexible characteristics are pretty similar to human breast tissue. The transparent feature and the coloring capability of water makes it possible to visualize the inner lesions in the breast phantoms. Moreover, the easy access of water does not overcomplicate the procedure and water phantoms can be reused in different

experiments. Finally, liquid radiotracer can easily mix with water uniformly and completely. Saline bags can be attached on the anterior surface of the torso phantom and will be pulled downward by gravity when the phantom is turned over to a prone torso orientation. The shape of the breast phantom does not necessarily have to be exactly the same as a real breast, but it must simulate the general manner of a human breast under different setups conditions.

**Table 3: Breast phantom material test results.**

Material	Time of formation	Malleability (rate: 1~10)	Mobility (rate: 1~10)	Reusable	Fit for PET procedure	Pros & Cons
Slime	~4 min	6	3	Yes	Yes	Very short formation time, but lack of mobility.
Bolus	~12h	8	8	Yes	No	Very flexible but needs long time of formation. Does not fit for PET procedures.
Gelatin	~1h	3	7	No	Yes	Easy to go moldy, and hard for storage. Cannot be reused in the experiment.
Water	~30 min	10	9	Yes	Yes	Clear & easy to reuse but needs to be in a completely sealed container.

### **3.2 Reconstruction and Imaging Analyses**

PET/CT images were acquired for this project and sets of images through the breast regions are attached in Appendix 5~Appendix 9, for each phantom orientation

and imaging modality. For easy comparison, the scanning parameters, such as FOV and slice thickness, were adjusted to be the same for these two types of images (Table 2). They all have a  $50 \times 50 \text{ cm}^2$  FOV and a 3.26-mm slice thickness. Compared with supine PET images, prone PET images present several artifacts, which are further discussed in section 4.2.

### **3.2.1 General Analyses**

The pixel widths of PET and CT are 3.9 mm and 0.98 mm, respectively. CT images provide the structural information; thus, they help determine the actual boundary of the lesion spheres as well as the center of the ROI. 10-mm spheres are relatively obvious in the CT images, whereas 8-mm spheres are harder to visualize, because the plastic material did not present a good contrast with water in CT, plus the influence of the existence of small air bubbles in the saline bag and around the spheres themselves further compounded the problem.

To be more specific, the same profile that passes through the center of a lesion sphere is obtained from both CT and PET image matrices (Figure 12). The values in both profiles are normalized to 1.0 to be evaluated, and the x-axis reflects the real distance from the center. The profile from CT is compressed within a small range due to the limited contrast; the top-most two peaks on both sides correspond to the location of the acrylic shell of the sphere. The profile from PET, however, presents a much broader peak in the image because of partial volume effect (PVE), which means the activity

within the ROI is spilled out to the surrounding background, and vice versa. The PVE is obvious especially when the dimension of the sphere is close to the limit that the PET scanner can resolve [34], resulting in a spot whose dimension is larger than the real size of the sphere in the reconstructed image.

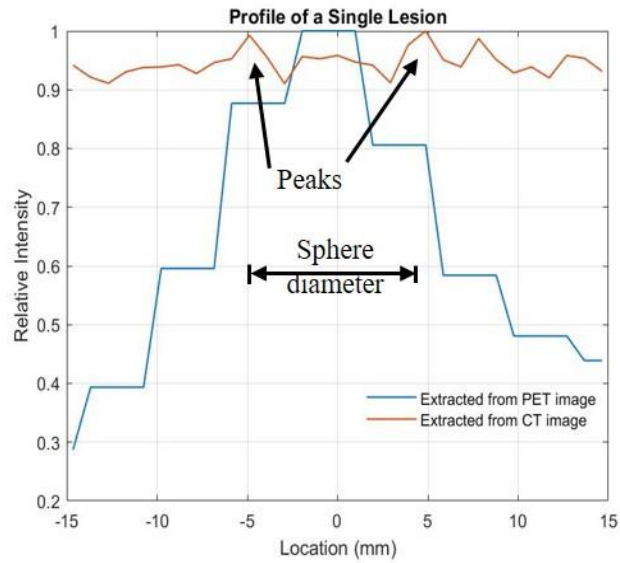


**Figure 12: Profiles extracted from PET and CT matrices.**

### 3.2.2 PET image reconstruction with varying time intervals

The images reconstructed with varying time intervals are not used for quantitative comparison and will not be discussed in detail in this section. However, these images can be used to study artifacts. For example, Figure 13 and Figure 14 show the same image slice in prone and supine phantom orientations with the reconstruction times labeled below. It is easy to tell that the images become less and less noisy as the reconstruction time-window increases. With the shorter reconstruction times the

structural artifacts, which appear to be bright streaks in the background especially between lesions, are not as easily apparent as with longer reconstruction times. As these bright streaks only appear between lesions, they may be artifacts that arise during reconstruction due to the presence of two large lesions with high signals on the same plane. This is unlikely to occur in a patient, however, so the same type of structural artifact might not appear in patient images. There are additional, low-signal streak-like artifacts that are also not as easily visible in the higher noise, shorter reconstruction time images.

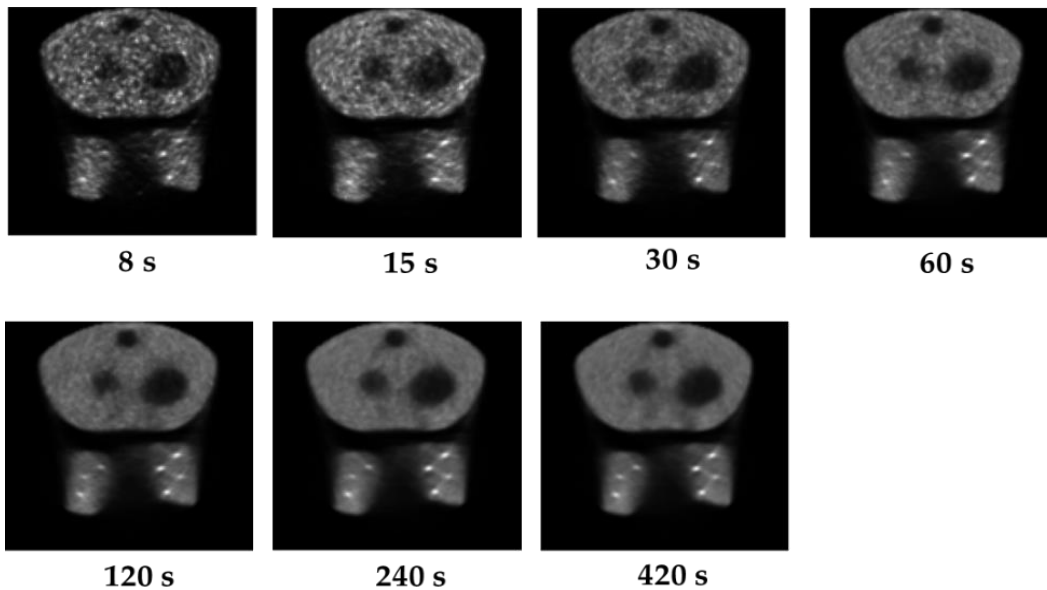


**Figure 13: Prone PET images reconstructed over varying time intervals.**

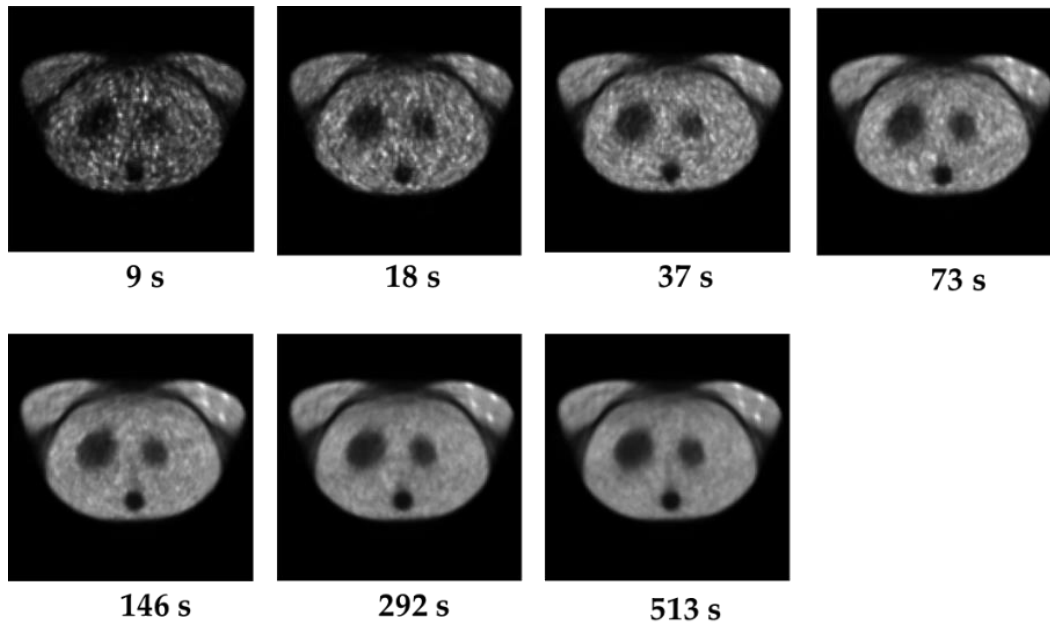


**Figure 14: Supine PET images reconstructed over varying time intervals. Time intervals are longer here than for the prone data in Figure 13 to partially compensate for radioactive decay.**

### **3.2.3 PET image reconstruction with equal time intervals**

For complete results, Table 4~11 list values of average signal and background in terms of different lesion sizes (8 mm and 10 mm) from both prone and supine PET images reconstructed with equal time intervals (90 s for prone and 110 s for supine).

There are 10 realizations of each reconstructed condition effectively yielding independent (uncorrelated) measurements with the same time acquisition. Theoretically, there should not be big differences in the VOI average values across the 10 frames because the data are reconstructed identically, and the time of decay and random events

only cause little variation in the expected values. The following comparison metrics (subsections 3.2.4 ~ 3.2.9) are based on the results in this section.

**Table 4: Average signal of 8 VOIs throughout equal time intervals (8 mm spheres, prone, units in 10<sup>4</sup> Bq/mL)<sup>1</sup>**

<b>Lesion # / Time frame (min)</b>	<b>1</b>	<b>2</b>	<b>3</b>	<b>4</b>	<b>5</b>	<b>6</b>	<b>7</b>	<b>8</b>	<b>AVG±STD over 8 lesions</b>	<b>STD% over 8 lesions</b>
<b>0~1.5</b>	1.42	1.21	1.24	1.06	1.03	1.10	1.20	1.35	1.20±0.14	11.37%
<b>1.5~3</b>	1.42	1.22	1.33	1.05	1.05	1.14	1.22	1.42	1.23±0.15	12.02%
<b>3~4.5</b>	1.39	1.20	1.29	1.07	1.00	1.08	1.18	1.40	1.20±0.15	12.46%
<b>4.5~6</b>	1.44	1.23	1.31	1.03	0.96	1.12	1.25	1.40	1.22±0.17	14.04%
<b>6~7.5</b>	1.37	1.22	1.29	1.13	1.04	1.15	1.18	1.39	1.22±0.12	10.01%
<b>7.5~9</b>	1.43	1.21	1.31	1.06	1.06	1.11	1.19	1.40	1.22±0.15	12.04%
<b>9~10.5</b>	1.38	1.23	1.34	1.07	0.98	1.14	1.13	1.38	1.21±0.15	12.57%
<b>10.5~12</b>	1.40	1.21	1.32	1.04	1.07	1.12	1.19	1.40	1.22±0.14	11.66%
<b>12~13.5</b>	1.46	1.13	1.23	1.07	1.04	1.16	1.17	1.38	1.20±0.15	12.14%
<b>13.5~15</b>	1.41	1.15	1.26	1.02	1.05	1.13	1.30	1.36	1.21±0.14	11.84%
<b>AVE±STD over 10 frames</b>	1.41±0.03	1.20±0.03	1.29±0.04	1.06±0.03	1.03±0.04	1.12±0.02	1.20±0.05	1.39±0.02	N/A	
<b>STD% over 10 frames</b>	1.84%	2.79%	2.83%	2.77%	3.54%	2.03%	3.78%	1.51%		

43

<sup>1</sup> Note: "AVG±STD" and "STD%" in the right columns corresponds to average/(percentage) standard deviation across 8 lesions, whereas "AVG±STD" and "STD%" in the bottom rows corresponds to average/(percentage) standard deviation across 10 time-frames (measurements). Same principle applies to the next following tables.

**Table 5: Average background ( $\pm\text{STD}_{bkg}$ ) of 8 VOIs throughout equal time intervals (8 mm spheres, prone, units in  $10^4$  Bq/mL)**

Lesion # / Time frame (min)	1	2	3	4	5	6	7	8	AVG $\pm$ STD over 8 lesions	STD% over 8 lesions
0~1.5	0.85 $\pm$ 0.10	0.73 $\pm$ 0.11	0.75 $\pm$ 0.13	0.66 $\pm$ 0.11	0.66 $\pm$ 0.13	0.62 $\pm$ 0.13	0.81 $\pm$ 0.09	0.92 $\pm$ 0.10	0.75 $\pm$ 0.10	13.77%
1.5~3	0.90 $\pm$ 0.09	0.72 $\pm$ 0.11	0.75 $\pm$ 0.13	0.67 $\pm$ 0.11	0.68 $\pm$ 0.12	0.62 $\pm$ 0.12	0.81 $\pm$ 0.09	0.93 $\pm$ 0.11	0.76 $\pm$ 0.11	14.63%
3~4.5	0.90 $\pm$ 0.09	0.74 $\pm$ 0.10	0.77 $\pm$ 0.13	0.67 $\pm$ 0.11	0.67 $\pm$ 0.12	0.62 $\pm$ 0.13	0.80 $\pm$ 0.10	0.92 $\pm$ 0.12	0.76 $\pm$ 0.11	14.54%
4.5~6	0.92 $\pm$ 0.09	0.72 $\pm$ 0.11	0.77 $\pm$ 0.13	0.67 $\pm$ 0.11	0.69 $\pm$ 0.13	0.63 $\pm$ 0.12	0.80 $\pm$ 0.10	0.93 $\pm$ 0.10	0.77 $\pm$ 0.11	14.51%
6~7.5	0.91 $\pm$ 0.10	0.72 $\pm$ 0.12	0.76 $\pm$ 0.13	0.68 $\pm$ 0.11	0.69 $\pm$ 0.11	0.64 $\pm$ 0.11	0.78 $\pm$ 0.09	0.94 $\pm$ 0.12	0.77 $\pm$ 0.11	14.10%
7.5~9	0.89 $\pm$ 0.10	0.72 $\pm$ 0.10	0.76 $\pm$ 0.13	0.67 $\pm$ 0.10	0.67 $\pm$ 0.14	0.63 $\pm$ 0.12	0.81 $\pm$ 0.11	0.91 $\pm$ 0.11	0.76 $\pm$ 0.11	13.91%
9~10.5	0.91 $\pm$ 0.10	0.72 $\pm$ 0.11	0.75 $\pm$ 0.13	0.67 $\pm$ 0.10	0.68 $\pm$ 0.12	0.63 $\pm$ 0.14	0.80 $\pm$ 0.09	0.90 $\pm$ 0.10	0.76 $\pm$ 0.11	14.11%
10.5~12	0.90 $\pm$ 0.11	0.73 $\pm$ 0.12	0.78 $\pm$ 0.14	0.69 $\pm$ 0.11	0.70 $\pm$ 0.12	0.64 $\pm$ 0.12	0.80 $\pm$ 0.09	0.94 $\pm$ 0.10	0.77 $\pm$ 0.10	13.56%
12~13.5	0.93 $\pm$ 0.10	0.73 $\pm$ 0.11	0.75 $\pm$ 0.13	0.69 $\pm$ 0.09	0.67 $\pm$ 0.12	0.63 $\pm$ 0.13	0.81 $\pm$ 0.09	0.92 $\pm$ 0.10	0.76 $\pm$ 0.11	14.47%
13.5~15	0.91 $\pm$ 0.09	0.72 $\pm$ 0.10	0.75 $\pm$ 0.13	0.67 $\pm$ 0.11	0.69 $\pm$ 0.12	0.64 $\pm$ 0.11	0.79 $\pm$ 0.10	0.92 $\pm$ 0.10	0.76 $\pm$ 0.11	14.01%
AVE $\pm$ STD over 10 frames	0.90 $\pm$ 0.02	0.73 $\pm$ 0.01	0.76 $\pm$ 0.01	0.68 $\pm$ 0.01	0.68 $\pm$ 0.01	0.63 $\pm$ 0.01	0.80 $\pm$ 0.01	0.92 $\pm$ 0.01	N/A	
STD% over 10 frames	2.19%	0.91%	1.39%	1.47%	1.88%	1.26%	1.11%	1.18%		

**Table 6: Average signal of 8 VOIs throughout equal time intervals (10 mm spheres, prone, units in 10<sup>4</sup> Bq/mL)**

<b>Lesion # / Time frame (min)</b>	<b>1</b>	<b>2</b>	<b>3</b>	<b>4</b>	<b>5</b>	<b>6</b>	<b>7</b>	<b>8</b>	<b>AVG±STD over 8 lesions</b>	<b>STD% over 8 lesions</b>
<b>0~1.5</b>	1.65	1.41	1.54	1.71	1.35	1.57	1.60	1.58	1.55±0.12	7.75%
<b>1.5~3</b>	1.66	1.39	1.52	1.64	1.26	1.51	1.58	1.70	1.53±0.15	9.63%
<b>3~4.5</b>	1.62	1.40	1.52	1.71	1.29	1.49	1.63	1.68	1.54±0.14	9.31%
<b>4.5~6</b>	1.65	1.44	1.53	1.66	1.29	1.49	1.55	1.72	1.54±0.14	9.05%
<b>6~7.5</b>	1.68	1.50	1.54	1.71	1.31	1.49	1.65	1.62	1.56±0.13	8.31%
<b>7.5~9</b>	1.72	1.45	1.56	1.71	1.29	1.56	1.59	1.65	1.57±0.14	9.09%
<b>9~10.5</b>	1.59	1.48	1.50	1.68	1.33	1.59	1.55	1.70	1.55±0.12	7.57%
<b>10.5~12</b>	1.70	1.41	1.55	1.64	1.24	1.51	1.52	1.65	1.53±0.15	9.85%
<b>12~13.5</b>	1.66	1.42	1.55	1.69	1.35	1.53	1.57	1.67	1.55±0.12	7.72%
<b>13.5~15</b>	1.67	1.43	1.56	1.64	1.32	1.53	1.54	1.61	1.54±0.12	7.50%
<b>AVE±STD over 10 frames</b>	1.66±0.04	1.43±0.04	1.54±0.02	1.68±0.03	1.30±0.04	1.53±0.04	1.58±0.04	1.66±0.04	<b>N/A</b>	
<b>STD% over 10 frames</b>	2.20%	2.50%	1.40%	1.75%	2.73%	2.38%	2.49%	2.63%		

**Table 7: Average background ( $\pm\text{STD}_{bkg}$ ) of 8 VOIs throughout equal time intervals (10 mm spheres, prone, units in  $10^4$  Bq/mL)**

Lesion # / Time frame (min)	1	2	3	4	5	6	7	8	AVG $\pm$ STD over 8 lesions	STD% over 8 lesions
0~1.5	0.75 $\pm$ 0.12	0.63 $\pm$ 0.12	0.73 $\pm$ 0.13	0.82 $\pm$ 0.11	0.56 $\pm$ 0.12	0.71 $\pm$ 0.12	0.73 $\pm$ 0.17	0.78 $\pm$ 0.12	0.71 $\pm$ 0.08	11.40%
1.5~3	0.76 $\pm$ 0.12	0.61 $\pm$ 0.11	0.75 $\pm$ 0.13	0.81 $\pm$ 0.11	0.57 $\pm$ 0.13	0.69 $\pm$ 0.12	0.74 $\pm$ 0.16	0.78 $\pm$ 0.11	0.71 $\pm$ 0.08	11.71%
3~4.5	0.75 $\pm$ 0.13	0.61 $\pm$ 0.11	0.74 $\pm$ 0.14	0.82 $\pm$ 0.12	0.56 $\pm$ 0.13	0.71 $\pm$ 0.12	0.74 $\pm$ 0.16	0.78 $\pm$ 0.12	0.71 $\pm$ 0.09	11.97%
4.5~6	0.76 $\pm$ 0.12	0.62 $\pm$ 0.12	0.75 $\pm$ 0.13	0.83 $\pm$ 0.12	0.57 $\pm$ 0.12	0.72 $\pm$ 0.11	0.73 $\pm$ 0.17	0.79 $\pm$ 0.12	0.72 $\pm$ 0.09	11.92%
6~7.5	0.75 $\pm$ 0.12	0.62 $\pm$ 0.12	0.74 $\pm$ 0.13	0.83 $\pm$ 0.12	0.58 $\pm$ 0.12	0.70 $\pm$ 0.11	0.72 $\pm$ 0.17	0.78 $\pm$ 0.14	0.72 $\pm$ 0.08	11.65%
7.5~9	0.75 $\pm$ 0.11	0.62 $\pm$ 0.11	0.74 $\pm$ 0.12	0.83 $\pm$ 0.12	0.56 $\pm$ 0.12	0.70 $\pm$ 0.13	0.72 $\pm$ 0.16	0.79 $\pm$ 0.11	0.71 $\pm$ 0.09	12.34%
9~10.5	0.75 $\pm$ 0.12	0.61 $\pm$ 0.10	0.74 $\pm$ 0.12	0.83 $\pm$ 0.11	0.55 $\pm$ 0.12	0.70 $\pm$ 0.13	0.74 $\pm$ 0.17	0.77 $\pm$ 0.12	0.71 $\pm$ 0.09	12.38%
10.5~12	0.76 $\pm$ 0.12	0.64 $\pm$ 0.11	0.75 $\pm$ 0.13	0.83 $\pm$ 0.11	0.57 $\pm$ 0.11	0.71 $\pm$ 0.12	0.75 $\pm$ 0.17	0.78 $\pm$ 0.14	0.72 $\pm$ 0.08	11.48%
12~13.5	0.76 $\pm$ 0.11	0.63 $\pm$ 0.11	0.74 $\pm$ 0.12	0.83 $\pm$ 0.12	0.57 $\pm$ 0.13	0.71 $\pm$ 0.13	0.74 $\pm$ 0.18	0.78 $\pm$ 0.13	0.72 $\pm$ 0.08	11.61%
13.5~15	0.76 $\pm$ 0.13	0.62 $\pm$ 0.11	0.73 $\pm$ 0.14	0.83 $\pm$ 0.12	0.56 $\pm$ 0.12	0.71 $\pm$ 0.12	0.74 $\pm$ 0.17	0.78 $\pm$ 0.12	0.72 $\pm$ 0.08	11.82%
AVE $\pm$ STD over 10 frames	0.76 $\pm$ 0.01	0.62 $\pm$ 0.01	0.74 $\pm$ 0.01	0.82 $\pm$ 0.01	0.57 $\pm$ 0.01	0.71 $\pm$ 0.01	0.73 $\pm$ 0.01	0.78 $\pm$ 0.00	N/A	
STD% over 10 frames	0.76%	1.55%	0.93%	0.75%	1.18%	1.17%	1.13%	0.63%		

**Table 8: Average signal of 8 VOIs throughout equal time intervals (8 mm spheres, supine, units in 10<sup>4</sup> Bq/mL)**

<b>Lesion # / Time frame (min)</b>	<b>1</b>	<b>2</b>	<b>3</b>	<b>4</b>	<b>5</b>	<b>6</b>	<b>7</b>	<b>8</b>	<b>AVG±STD over 8 lesions</b>	<b>STD% over 8 lesions</b>
<b>0~1.5</b>	0.92	0.99	1.06	0.99	0.91	0.97	1.00	1.01	0.98±0.05	5.15%
<b>1.5~3</b>	0.94	1.02	1.10	1.01	0.93	1.01	1.01	0.97	1.00±0.05	5.14%
<b>3~4.5</b>	0.95	1.00	1.06	0.97	0.92	0.93	1.00	1.00	0.98±0.05	4.68%
<b>4.5~6</b>	0.96	1.02	1.06	1.06	0.93	0.97	0.99	1.03	1.00±0.05	4.83%
<b>6~7.5</b>	0.88	0.94	1.09	1.01	0.95	0.88	0.97	0.97	0.96±0.07	6.98%
<b>7.5~9</b>	0.93	1.00	1.07	0.96	0.98	0.96	0.93	1.00	0.98±0.04	4.54%
<b>9~10.5</b>	0.93	0.99	1.08	0.95	0.99	0.94	0.99	1.02	0.99±0.05	4.88%
<b>10.5~12</b>	0.98	0.98	1.11	0.93	0.95	0.93	0.99	0.98	0.98±0.06	5.82%
<b>12~13.5</b>	0.97	1.01	1.07	1.01	0.98	0.93	1.00	0.99	0.99±0.04	3.88%
<b>13.5~15</b>	1.00	1.00	1.07	0.97	1.00	0.91	0.97	0.98	0.99±0.04	4.42%
<b>AVE±STD over 10 frames</b>	0.95±0.03	1.00±0.02	1.08±0.02	0.99±0.04	0.96±0.03	0.94±0.03	0.98±0.02	0.99±0.02	<b>N/A</b>	
<b>STD% over 10 frames</b>	3.63%	2.25%	1.60%	3.90%	3.40%	3.65%	2.20%	1.98%		

**Table 9: Average background ( $\pm\text{STD}_{bkg}$ ) of 8 VOIs throughout equal time intervals (8 mm spheres, supine, units in  $10^4$  Bq/mL)**

Lesion # / Time frame (min)	1	2	3	4	5	6	7	8	AVG $\pm$ STD over 8 lesions	STD% over 8 lesions
0~1.5	0.69 $\pm$ 0.08	0.72 $\pm$ 0.10	0.62 $\pm$ 0.24	0.71 $\pm$ 0.11	0.65 $\pm$ 0.08	0.75 $\pm$ 0.08	0.58 $\pm$ 0.28	0.60 $\pm$ 0.26	0.66 $\pm$ 0.06	9.06%
1.5~3	0.69 $\pm$ 0.10	0.72 $\pm$ 0.10	0.61 $\pm$ 0.24	0.73 $\pm$ 0.12	0.66 $\pm$ 0.09	0.78 $\pm$ 0.08	0.59 $\pm$ 0.29	0.59 $\pm$ 0.26	0.67 $\pm$ 0.07	10.48%
3~4.5	0.69 $\pm$ 0.08	0.71 $\pm$ 0.10	0.61 $\pm$ 0.25	0.70 $\pm$ 0.12	0.66 $\pm$ 0.09	0.74 $\pm$ 0.09	0.59 $\pm$ 0.29	0.60 $\pm$ 0.27	0.66 $\pm$ 0.06	8.63%
4.5~6	0.68 $\pm$ 0.09	0.72 $\pm$ 0.10	0.62 $\pm$ 0.25	0.70 $\pm$ 0.11	0.67 $\pm$ 0.10	0.73 $\pm$ 0.07	0.58 $\pm$ 0.28	0.60 $\pm$ 0.28	0.66 $\pm$ 0.06	8.71%
6~7.5	0.69 $\pm$ 0.08	0.73 $\pm$ 0.10	0.62 $\pm$ 0.24	0.70 $\pm$ 0.11	0.66 $\pm$ 0.08	0.73 $\pm$ 0.08	0.58 $\pm$ 0.29	0.57 $\pm$ 0.26	0.66 $\pm$ 0.06	9.47%
7.5~9	0.71 $\pm$ 0.08	0.72 $\pm$ 0.11	0.61 $\pm$ 0.24	0.71 $\pm$ 0.10	0.66 $\pm$ 0.09	0.75 $\pm$ 0.07	0.58 $\pm$ 0.29	0.59 $\pm$ 0.27	0.67 $\pm$ 0.07	9.85%
9~10.5	0.69 $\pm$ 0.07	0.73 $\pm$ 0.11	0.62 $\pm$ 0.26	0.72 $\pm$ 0.12	0.66 $\pm$ 0.09	0.74 $\pm$ 0.08	0.59 $\pm$ 0.30	0.59 $\pm$ 0.27	0.67 $\pm$ 0.06	9.44%
10.5~12	0.69 $\pm$ 0.07	0.73 $\pm$ 0.11	0.61 $\pm$ 0.26	0.69 $\pm$ 0.12	0.66 $\pm$ 0.08	0.74 $\pm$ 0.07	0.59 $\pm$ 0.29	0.58 $\pm$ 0.28	0.66 $\pm$ 0.06	9.09%
12~13.5	0.69 $\pm$ 0.07	0.74 $\pm$ 0.12	0.61 $\pm$ 0.25	0.71 $\pm$ 0.11	0.66 $\pm$ 0.08	0.73 $\pm$ 0.06	0.58 $\pm$ 0.29	0.58 $\pm$ 0.27	0.66 $\pm$ 0.06	9.72%
13.5~15	0.69 $\pm$ 0.08	0.72 $\pm$ 0.12	0.61 $\pm$ 0.26	0.71 $\pm$ 0.11	0.67 $\pm$ 0.09	0.74 $\pm$ 0.07	0.60 $\pm$ 0.31	0.59 $\pm$ 0.29	0.67 $\pm$ 0.06	8.96%
AVE $\pm$ STD over 10 frames	0.69 $\pm$ 0.01	0.73 $\pm$ 0.01	0.61 $\pm$ 0.00	0.71 $\pm$ 0.01	0.66 $\pm$ 0.01	0.74 $\pm$ 0.01	0.59 $\pm$ 0.01	0.59 $\pm$ 0.01	N/A	
STD% over 10 frames	1.02%	1.05%	0.65%	1.37%	1.11%	1.89%	1.27%	1.67%		

**Table 10: Average signal of 8 VOIs throughout equal time intervals (10 mm spheres, supine, units in 10<sup>4</sup> Bq/mL)**

<b>Lesion # / Time frame (min)</b>	<b>1</b>	<b>2</b>	<b>3</b>	<b>4</b>	<b>5</b>	<b>6</b>	<b>7</b>	<b>8</b>	<b>AVG±STD over 8 lesions</b>	<b>STD% over 8 lesions</b>
<b>0~1.5</b>	1.07	1.10	1.25	1.28	1.18	1.24	1.24	1.25	1.20±0.08	6.32%
<b>1.5~3</b>	1.03	1.16	1.26	1.20	1.13	1.19	1.24	1.17	1.17±0.07	6.15%
<b>3~4.5</b>	1.01	1.17	1.29	1.26	1.15	1.18	1.26	1.28	1.20±0.09	7.77%
<b>4.5~6</b>	1.07	1.12	1.26	1.24	1.10	1.21	1.22	1.26	1.18±0.08	6.51%
<b>6~7.5</b>	1.06	1.16	1.25	1.23	1.13	1.18	1.29	1.29	1.20±0.08	6.94%
<b>7.5~9</b>	1.04	1.15	1.24	1.25	1.17	1.22	1.25	1.26	1.19±0.08	6.31%
<b>9~10.5</b>	1.00	1.13	1.19	1.18	1.11	1.20	1.23	1.27	1.16±0.08	7.11%
<b>10.5~12</b>	1.05	1.15	1.27	1.26	1.18	1.22	1.20	1.29	1.20±0.08	6.41%
<b>12~13.5</b>	1.03	1.11	1.24	1.25	1.12	1.19	1.21	1.21	1.17±0.07	6.37%
<b>13.5~15</b>	1.05	1.11	1.21	1.25	1.17	1.21	1.24	1.20	1.18±0.07	5.88%
<b>AVE±STD over 10 frames</b>	1.04±0.02	1.14±0.02	1.25±0.03	1.24±0.03	1.14±0.03	1.20±0.02	1.24±0.02	1.25±0.04	N/A	
<b>STD% over 10 frames</b>	2.22%	1.98%	2.19%	2.34%	2.67%	1.71%	2.00%	3.30%		

**Table 11: Average background ( $\pm\text{STD}_{bkg}$ ) of 8 VOIs throughout equal time intervals (10 mm spheres, supine, units in  $10^4$  Bq/mL)**

Lesion # / Time frame (min)	1	2	3	4	5	6	7	8	AVG $\pm$ STD over 8 lesions	STD% over 8 lesions
0~1.5	0.73 $\pm$ 0.06	0.61 $\pm$ 0.10	0.55 $\pm$ 0.27	0.56 $\pm$ 0.27	0.70 $\pm$ 0.10	0.71 $\pm$ 0.12	0.57 $\pm$ 0.29	0.62 $\pm$ 0.22	0.63 $\pm$ 0.07	11.16%
1.5~3	0.73 $\pm$ 0.07	0.59 $\pm$ 0.10	0.55 $\pm$ 0.28	0.54 $\pm$ 0.27	0.68 $\pm$ 0.09	0.70 $\pm$ 0.11	0.58 $\pm$ 0.29	0.62 $\pm$ 0.22	0.63 $\pm$ 0.07	11.51%
3~4.5	0.73 $\pm$ 0.06	0.59 $\pm$ 0.10	0.54 $\pm$ 0.27	0.56 $\pm$ 0.27	0.68 $\pm$ 0.09	0.70 $\pm$ 0.12	0.57 $\pm$ 0.30	0.62 $\pm$ 0.22	0.62 $\pm$ 0.07	11.31%
4.5~6	0.73 $\pm$ 0.07	0.60 $\pm$ 0.10	0.55 $\pm$ 0.27	0.55 $\pm$ 0.26	0.69 $\pm$ 0.10	0.70 $\pm$ 0.13	0.59 $\pm$ 0.30	0.63 $\pm$ 0.22	0.63 $\pm$ 0.07	11.18%
6~7.5	0.73 $\pm$ 0.07	0.60 $\pm$ 0.11	0.56 $\pm$ 0.29	0.57 $\pm$ 0.27	0.67 $\pm$ 0.10	0.70 $\pm$ 0.12	0.60 $\pm$ 0.31	0.64 $\pm$ 0.23	0.63 $\pm$ 0.06	9.78%
7.5~9	0.73 $\pm$ 0.07	0.60 $\pm$ 0.10	0.55 $\pm$ 0.27	0.58 $\pm$ 0.26	0.68 $\pm$ 0.10	0.70 $\pm$ 0.13	0.59 $\pm$ 0.31	0.62 $\pm$ 0.22	0.63 $\pm$ 0.06	10.03%
9~10.5	0.72 $\pm$ 0.07	0.61 $\pm$ 0.10	0.55 $\pm$ 0.28	0.58 $\pm$ 0.26	0.69 $\pm$ 0.09	0.71 $\pm$ 0.13	0.57 $\pm$ 0.30	0.63 $\pm$ 0.21	0.63 $\pm$ 0.07	10.36%
10.5~12	0.73 $\pm$ 0.05	0.60 $\pm$ 0.10	0.56 $\pm$ 0.28	0.57 $\pm$ 0.26	0.70 $\pm$ 0.08	0.71 $\pm$ 0.14	0.60 $\pm$ 0.31	0.63 $\pm$ 0.22	0.64 $\pm$ 0.07	10.58%
12~13.5	0.74 $\pm$ 0.07	0.61 $\pm$ 0.10	0.55 $\pm$ 0.29	0.58 $\pm$ 0.26	0.67 $\pm$ 0.09	0.70 $\pm$ 0.13	0.60 $\pm$ 0.31	0.61 $\pm$ 0.21	0.63 $\pm$ 0.06	10.11%
13.5~15	0.73 $\pm$ 0.06	0.60 $\pm$ 0.10	0.55 $\pm$ 0.28	0.58 $\pm$ 0.26	0.68 $\pm$ 0.09	0.70 $\pm$ 0.13	0.60 $\pm$ 0.31	0.60 $\pm$ 0.21	0.63 $\pm$ 0.06	10.13%
AVE $\pm$ STD over 10 frames	0.73 $\pm$ 0.01	0.60 $\pm$ 0.01	0.55 $\pm$ 0.01	0.57 $\pm$ 0.01	0.68 $\pm$ 0.01	0.70 $\pm$ 0.00	0.59 $\pm$ 0.01	0.62 $\pm$ 0.01	N/A	
STD% over 10 frames	0.77%	0.93%	0.93%	2.46%	1.34%	0.65%	2.06%	1.61%		

### 3.2.4 Comparison Metrics—average signal and background

Based on the results of 10 measurements, Figure 15 shows the mean values of the average signal intensity as well as background calculated for each lesion in both prone and supine positions (also tabulated in Table 12). The estimated background values were close to the expected values, which were calculated from the known initial activity and corrected for decay. The upper pair of solid curves (red for 8 mm spheres and blue for 10 mm spheres) are average values of VOIs, and the lower pair of dashed curves with error bars demonstrates the corresponding background with noise. As a result, the average signal and background are more uniform in supine than prone orientation, which is a drawback of the prone setup. A possible explanation for this could be the different location of the breasts relative to the field of view. In supine position, the breasts are closer to the center field of view, whereas in prone position the breasts are located at a relatively low position away from the center FOV, yielding the variation in the calculated averages. Additionally, in the supine position, there is greater noise in the average backgrounds (e.g. lesions 3, 4, 7, and 8 for 10-mm spheres in Table 12) than other lesions, because the locations of these four lesions are close to the breast surface where edge blur is more influential. For both prone and supine orientations, the standard deviation of the average signal across 10 individual lesion measurements are always smaller than the standard deviation across 8 lesions because the latter not only includes the statistical noise, but also includes the non-uniformity in the reconstructed

images. On the other hand, the overall signals in prone position are higher than supine because of the signal intensity loss from decay. As there is an approximate 30 min time interval between prone and supine acquisitions, and considering the half-life of  $^{18}\text{F}$ , then  $1 - \left(\frac{1}{2}\right)^{30/109.7} \approx 0.173$  indicates that 17% of the radionuclides are decayed away in this time period, which approximately corresponds to the change in the average lesion signals, but not the corresponding background signals.

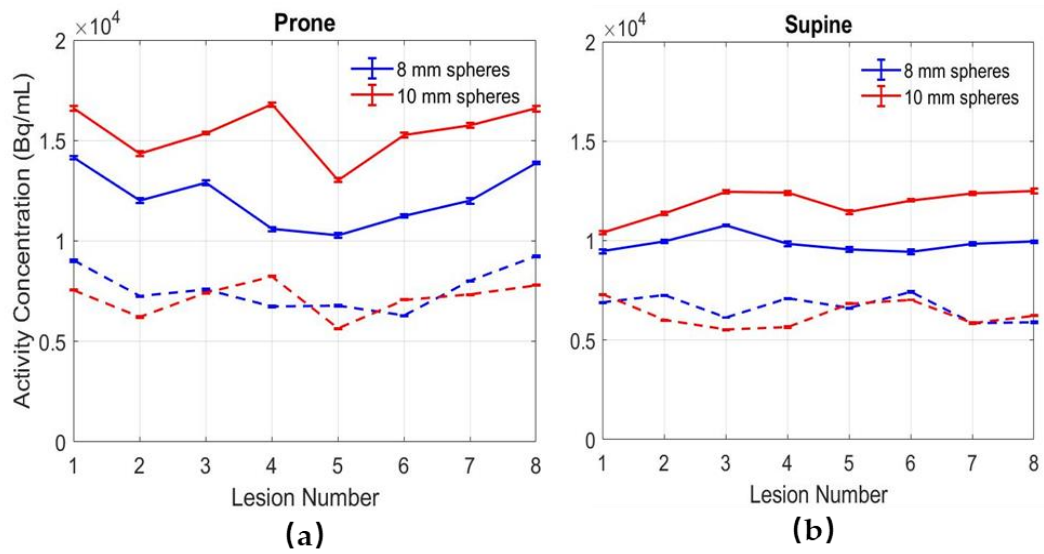


**Figure 15: Average signal (solid curve) and background (dashed curve) for each lesion sphere (mean values over 10 measurements). (a) Prone setup. (b) Supine setup.**

**Table 12: Average signal & background ( $\pm\text{STD}_{bkg}$ ) for each lesion sphere**

Lesions (Unit: $10^4$ Bq/mL)			1	2	3	4	5	6	7	8	Ensemble average over 8 lesions
VOI (mean $\pm\text{STD}$ over 10)	8 mm spheres	Prone	1.41 $\pm$ 0.03	1.20 $\pm$ 0.03	1.29 $\pm$ 0.04	1.06 $\pm$ 0.03	1.03 $\pm$ 0.04	1.12 $\pm$ 0.02	1.20 $\pm$ 0.05	1.39 $\pm$ 0.02	1.21 $\pm$ 0.14
		Supine	0.95 $\pm$ 0.03	1.00 $\pm$ 0.02	1.08 $\pm$ 0.02	0.99 $\pm$ 0.04	0.96 $\pm$ 0.03	0.94 $\pm$ 0.03	0.98 $\pm$ 0.02	0.99 $\pm$ 0.02	0.99 $\pm$ 0.04
	10 mm spheres	Prone	1.66 $\pm$ 0.04	1.43 $\pm$ 0.04	1.54 $\pm$ 0.02	1.68 $\pm$ 0.03	1.30 $\pm$ 0.04	1.53 $\pm$ 0.04	1.58 $\pm$ 0.04	1.66 $\pm$ 0.04	1.55 $\pm$ 0.13
		Supine	1.04 $\pm$ 0.02	1.14 $\pm$ 0.02	1.25 $\pm$ 0.03	1.24 $\pm$ 0.03	1.14 $\pm$ 0.03	1.20 $\pm$ 0.02	1.24 $\pm$ 0.02	1.25 $\pm$ 0.04	1.19 $\pm$ 0.07
BKG (mean $\pm\text{STD}$ over 10)	8 mm spheres	Prone	0.90 $\pm$ 0.10	0.73 $\pm$ 0.11	0.76 $\pm$ 0.13	0.68 $\pm$ 0.11	0.68 $\pm$ 0.12	0.63 $\pm$ 0.12	0.80 $\pm$ 0.09	0.92 $\pm$ 0.11	N/A
		Supine	0.69 $\pm$ 0.08	0.73 $\pm$ 0.11	0.61 $\pm$ 0.25	0.71 $\pm$ 0.11	0.66 $\pm$ 0.09	0.74 $\pm$ 0.07	0.59 $\pm$ 0.29	0.59 $\pm$ 0.27	
	10 mm spheres	Prone	0.76 $\pm$ 0.12	0.62 $\pm$ 0.11	0.74 $\pm$ 0.13	0.82 $\pm$ 0.11	0.57 $\pm$ 0.12	0.71 $\pm$ 0.12	0.73 $\pm$ 0.17	0.78 $\pm$ 0.12	
		Supine	0.73 $\pm$ 0.07	0.60 $\pm$ 0.10	0.55 $\pm$ 0.28	0.57 $\pm$ 0.27	0.68 $\pm$ 0.09	0.70 $\pm$ 0.12	0.59 $\pm$ 0.31	0.62 $\pm$ 0.22	

### 3.2.5 Comparison Metrics—SNR

Figure 16 shows the calculated signal-to-noise ratios (SNR) for each lesion in the breast phantoms (also tabulated in Table 13), and the standard error of SNR appears as the error bar in the figure. Clearly, the SNRs obtained from prone position are greater than the SNRs in supine position. Additionally, prone SNRs are more uniform than supine SNRs because there is more variation in the background pixels close to the breast surface. Another factor that may also have influence on SNRs is proximity to the torso background. In the supine position, the breasts rest on the surface of the torso, therefore, the scatter from the torso background may contribute to the breasts, resulting in a relatively noisier background for the breast.

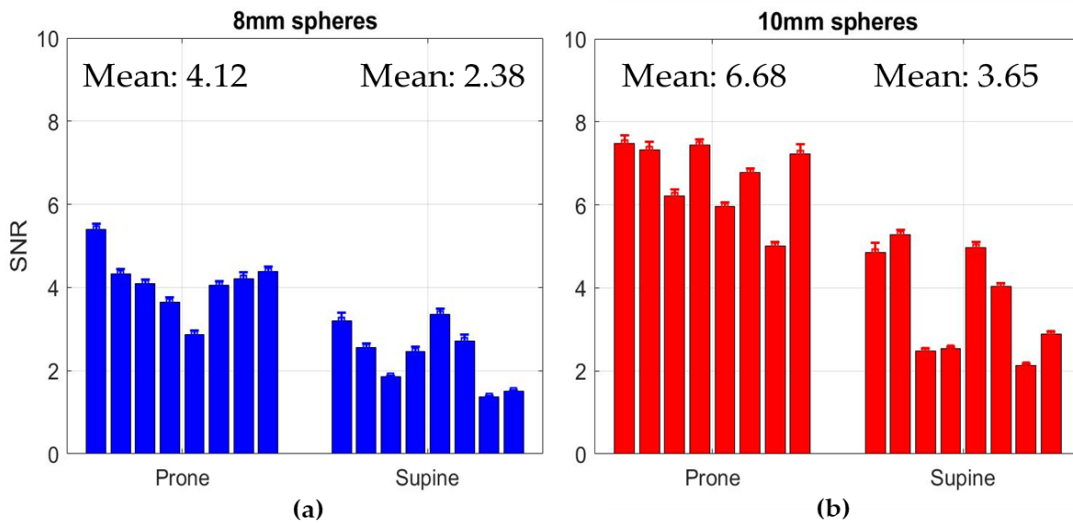


Figure 16: Average signal-to-noise ratios of each lesion sphere. (a) 8 mm spheres. (b) 10 mm spheres.

Table 13: Average SNR ( $\overline{\text{SNR}} \pm \Delta \text{SNR}$ ) of each lesion sphere

		1	2	3	4	5	6	7	8	AVG±STD over 8 lesions
8 mm spheres	Prone	5.40±0.47	4.33±0.38	4.09±0.30	3.65±0.35	2.87±0.34	4.05±0.31	4.21±0.51	4.39±0.33	4.12±0.67
	Supine	3.20±0.60	2.55±0.30	1.85±0.07	2.45±0.42	3.36±0.43	2.72±0.46	1.36±0.10	1.50±0.07	2.38±0.70
10 mm spheres	Prone	7.48±0.64	7.33±0.63	6.22±0.46	7.44±0.41	5.95±0.33	6.78±0.33	5.01±0.34	7.23±0.74	6.68±0.83
	Supine	4.85±0.76	5.28±0.36	2.49±0.14	2.54±0.11	4.97±0.47	4.05±0.25	2.14±0.12	2.89±0.18	3.65±1.20

### 3.2.6 Comparison Metrics—local contrast

Figure 17 is the local contrast calculated for each lesion sphere in the breast phantoms (also tabulated in Table 14), and the standard error of contrast appears as the error bar in the figure. Clearly, the 10 mm spheres present better local contrast than 8 mm spheres in both prone and supine setups. The change of the local contrast from prone to supine is not very obvious, but prone images present better local contrast than

supine images (though not statistically significant, as shown in section 3.2.8) when comparing the mean values of the two cases.

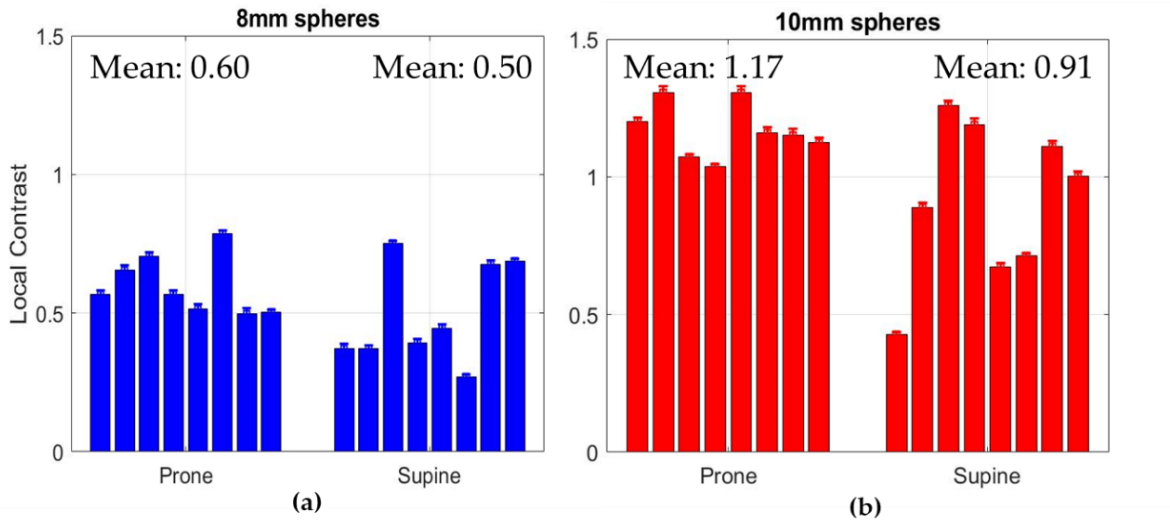


**Figure 17: Average local contrast of each lesion sphere. (a) 8 mm spheres. (b) 10 mm spheres.**

**Table 14: Average local contrast ( $\bar{C} \pm \Delta C$ ) of each lesion sphere**

		1	2	3	4	5	6	7	8	AVG $\pm$ STD over 8 lesions
8 mm spheres	Prone	0.57 $\pm$ 0.05	0.66 $\pm$ 0.05	0.70 $\pm$ 0.05	0.57 $\pm$ 0.05	0.51 $\pm$ 0.06	0.79 $\pm$ 0.04	0.50 $\pm$ 0.07	0.50 $\pm$ 0.03	0.60 $\pm$ 0.11
	Supine	0.37 $\pm$ 0.05	0.37 $\pm$ 0.04	0.75 $\pm$ 0.03	0.39 $\pm$ 0.06	0.45 $\pm$ 0.05	0.27 $\pm$ 0.03	0.68 $\pm$ 0.04	0.69 $\pm$ 0.03	0.50 $\pm$ 0.18
10 mm spheres	Prone	1.20 $\pm$ 0.05	1.31 $\pm$ 0.08	1.07 $\pm$ 0.03	1.04 $\pm$ 0.03	1.31 $\pm$ 0.07	1.16 $\pm$ 0.07	1.15 $\pm$ 0.07	1.13 $\pm$ 0.05	1.17 $\pm$ 0.10
	Supine	0.43 $\pm$ 0.03	0.89 $\pm$ 0.05	1.26 $\pm$ 0.06	1.19 $\pm$ 0.07	0.67 $\pm$ 0.05	0.71 $\pm$ 0.03	1.11 $\pm$ 0.06	1.00 $\pm$ 0.05	0.91 $\pm$ 0.29

### 3.2.7 Comparison Metrics—contrast uniformity

Contrast uniformity reflects the reliability of the contrast measurements and is calculated by taking the averaged standard deviation of the contrast for 8 lesions over 10 individual (i.e. replayed) measurements. Therefore, the lower the value of the contrast uniformity, the more uniform the contrast is throughout the breast. As the result shows in Table 15, for both 8 mm and 10 mm spheres, the contrast presents better uniformity in the prone orientation than the supine orientation.

**Table 15: Contrast uniformity**

	8 mm spheres		10 mm spheres	
	Prone	Supine	Prone	Supine
CU	0.114	0.185	0.110	0.290

### 3.2.8 Comparison Metrics—paired t-test

The calculated p-values for each prone vs supine comparison metric are tabulated in Table 16. As it shows in the table, the p-values of the lesion signal and the SNR comparisons are less than 0.05. Therefore, it can be concluded that there are significant differences between prone and supine images in terms of lesion signal and SNR for both 8 mm and 10 mm spheres.

**Table 16: Paired t-test (prone vs supine)**

	Lesion signal		SNR		Local contrast	
	8 mm spheres	10 mm spheres	8 mm spheres	10 mm spheres	8 mm spheres	10 mm spheres
<b>p-value</b>	0.00239	0.00013	0.00281	0.00026	0.26016	0.07818

## 4. Discussion

### 4.1 Caveats about the breast phantom materials

In general, there are three factors that have to be considered to evaluate the breast phantom materials for the purpose of this project. First, the material has to be malleable, which means it can be made into different breast shapes. All of the three materials (excluding water) are malleable to some extent. Second, the material should be flexible, in other words, it can change its shape automatically in different setups to simulate the manner of breast. It turns out that three materials have different degrees of flexibility, but there is some difficulty in storing these materials in a shapeable container that can change its shape without changing its volume. Third, the material should be suitable for PET procedures, which includes two aspects: its time of formation should be within the half-life of the radio isotope ( $^{18}\text{F}$ ) and it can form a uniform distribution once radioactivity is added. All of the three materials have their own advantages and disadvantages, and considering the purpose of this project, it is either not feasible to use the material to build up the breast phantom, or it overcomplicates imaging procedures. Water sealed in a plastic bag (container) turns out to be the easiest to work with, while satisfying the three criteria.

## ***4.2 Factors that influence image quality in prone and supine PET images***

Image pre-processing, which includes pixel replication and interpolation, is an important step in this project to obtain accurate results. Replication preserves the pixels' original values and interpolation assigns the pixel values with different weightings. To some extent, pixel interpolation increases the precision of average calculation by assigning the pixels covered by a ROI with different weightings in the calculation, especially when the size of the ROI is relatively small. As for the coarse pixels completely included in the ROI, replication does not have influence on the calculation. As an example, Figure 18 shows a diagram of four adjacent pixels with values of 1~4. Thus, their average is  $(1 + 2 + 3 + 4)/4 = 2.5$  and will be the same if assigned with the same weighting. If without pixel interpolation, the red and blue ROIs will have the same average value no matter how ROI is placed relative this matrix. However, it will be more reasonable if pixel 1 and pixel 4 are assigned with higher weightings to calculate the averages of red and blue ROIs. Therefore, pixel interpolation increases the precision when calculating the average.

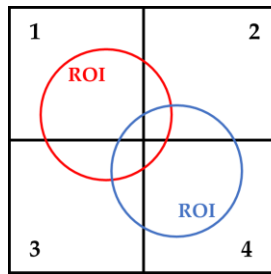


**Figure 18: Diagram to illustrate the effect of pixel replication versus interpolation on calculating average.**

There are several potential factors which can influence PET image quality in terms of prone versus supine position. First, the location of the breasts with regard to the field of view of the PET/CT scanner may influence detection efficiency. In the supine position, the torso takes up the center field of view, pushing the breasts bilaterally in the FOV, whereas in the prone position, the breasts locate in the lower edge of the FOV. In the supine position, some lesions are close to the anterior surface of the breast (blurred region), where it is more affected by blur at the edge. This is a limitation of the method to calculate the metrics using these spheres. Whereas in the prone position, none of the lesions locate really close to the breast boundary, which makes the calculated results more reliable than in the supine position. This may be an implementation flaw in the breast phantom because lesions are not known to move so radically in humans, and the shape of the phantom does not exactly imitate the human breast when changing from prone to supine positions. In the supine position, the torso background scatter may contribute noise to the breasts as they rest on the surface of the torso; whereas in the prone position, the breasts are about 10 cm away from the torso (even farther for the

anterior end of the breast). The factors mentioned above can cause different extents of image artifacts in prone versus supine images.

Second, the location of the lesion with respect to the image slices can result in variations in the calculated average signal values. As is shown in Figure 19, an 8 mm sphere occupies 3 consecutive slices, while a 10 mm sphere could occupy up to 4 consecutive slices. An assumption made during VOI creation is that the sphere is always located symmetrically with respect to the slices, so the radii of the circular ROIs in the images were scaled down by fixed factors. However, this assumption does not hold when the lesion sphere is not symmetrically located across the slices, which happens most of the time; most often, unequal fractions of the lesion are included in the starting and the ending slice. Using symmetric radius scaling factors would result in the creation of a VOI that is not well-aligned with the actual lesion and is thus inappropriate. Such a situation could be addressed in future iterations of this work by directly determining the VOI for each sphere from the CT images without any assumptions.

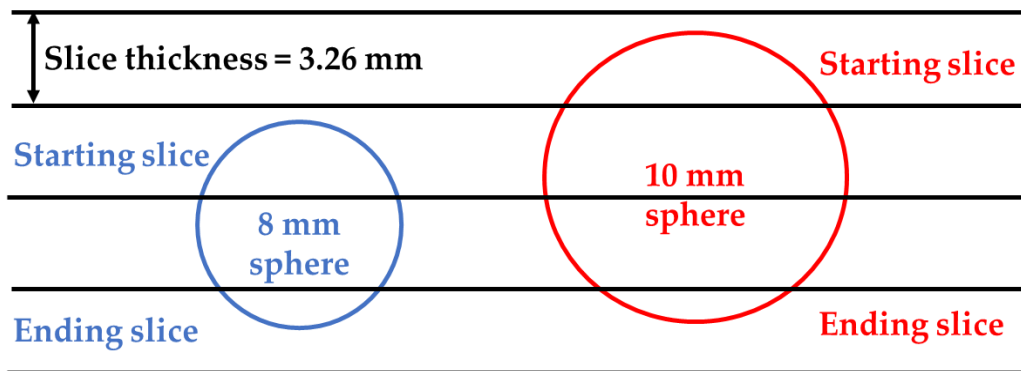


Figure 19: Diagram of the locations of the spheres with respect to the image slices.

Finally, the presence of artifacts distinguishes the image quality in different orientations. Although the images are reconstructed with attenuation and scatter correction, CT images in the prone and supine positions have different image qualities because some photons may experience longer paths (breast + torso) in prone position as compared to the supine position, resulting in the more obvious streak artifacts in the acquired CT images (Figure 20-a). The presence of the high density-plastic in the phantom which imitates the vertebrae can also cause beam hardening artifacts, and this artifact may also be present in a real patient. In the corresponding PET image (Figure 20-b), there is a defect at the edge of the lung probably because the breast moved a little bit between the PET and CT scans, as well as the imperfect attenuation and scatter correction from the CT image. Finally, the attenuation and scatter effect of the torso support may have small effects (Appendix 7), but this is not likely the main issue, because the foam support is made of quite a radiolucent material.

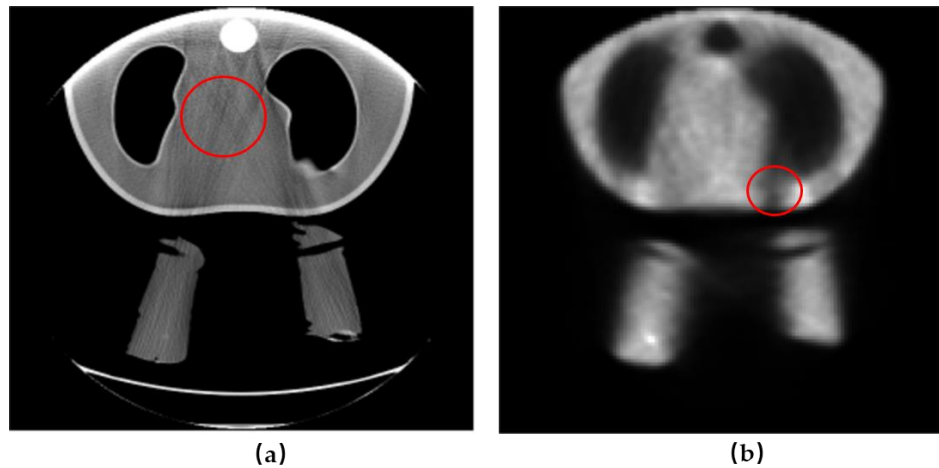


Figure 20: Example of artifacts in (a) CT image and (b) PET image caused by different factors.

### ***4.3 Noise calculation in different situations***

Although the same standard deviation formula is used to calculate the noise, it is actually applied in different situations and has different interpretations. In summary, there are three ways to calculate the noise. First, standard deviation can be applied to a VOI to calculate the pixel-by-pixel variation (Eqn. 2.2), which is herein referred to as the background noise in the definition of SNR. However, a limitation of this method is that it includes both non-random variations, such as non-uniformity due to partial volume effects, as well as to random fluctuations. Also, the pixel values in the reconstructed image are not independent variables, and the covariance terms which depend on the reconstruction algorithm (e.g. OSEM) are not easy to determine. Second, standard deviation can be used to quantify the variation of a metric, such as absolute activity or contrast or another metric, across different VOIs. An example is the contrast uniformity

(Eqn. 2.13) across 8 lesions. Last, standard deviation can be used to quantify the variation of a metric across different noisy realizations. Examples include the calculated standard deviations of SNR (Eqn. 2.5) and local contrast (Eqn. 2.9) across 10 measurements. In this situation, the standard deviation is reporting how repeatable the quantitative measurements are.

#### ***4.4 Resolution versus partial volume effect***

Resolution is the ability of an imaging system to accurately depict two distinct objects in space. In this project, it typically means the width of the lesion sphere imaged in the PET/CT scanner. Partial volume effect, on the other hand, is a combining effect that results from both poor resolution and image reconstruction. The radioactivity in the sphere can spill out to the nearby background, yielding a blurred spot larger than the real size of the object in the reconstructed PET image. Therefore, partial volume effect and resolution are closely related in PET imaging. The intrinsic resolution of a PET scanner, typically 5 mm, is determined by its detector size, positron range, and non-collinearity [35]. However, when considering the effects of image reconstruction and processing, the realized resolution of the PET system is even worse than 5 mm [34].

#### ***4.5 Pros and cons of prone versus supine setup in PET/CT imaging***

Based on calculated results, it turns out that prone breast PET imaging may have some advantages over supine breast PET imaging. From an image quality perspective,

prone PET images have better SNR and contrast uniformity than supine PET images. A limitation of this project is that only phantom studies are performed in this project, but in real patient scanning, the movement of the patient may cause uncertainties and degrade the image quality of both PET/CT.

In the supine setup, some lesions are really close to the surface of the breast, which makes them difficult to be localized, whereas it is easier to evaluate the lesions in prone setup because they are closer to the center of the breast in prone position. However, it will not be the same case for a real patient because the lesions inside the phantom may not move as far in real breasts. As a common clinical protocol, supine breast PET/CT imaging is easier to process, but the acquired image may be degraded due to the respirational movement of the patient's chest wall and the presence of unexpected image artifacts. On the other hand, the presence of the torso support in the prone setup may complicate the prone breast PET/CT imaging procedures and can cause discomfort to the patient, but the acquired images can be less affected by the movement because the patient's chest wall fixes to the support structure in the prone orientation and the patient's back raises and lowers during breathing.

## 5. Conclusions

In summary, prone breast PET/CT imaging with a clinical imaging system was investigated successfully using the developed torso support and saline bag breast phantoms. From the results and discussions above, it can be concluded that prone PET/CT imaging is geometrically feasible with the utilization of the developed torso support for patients of the phantom size or smaller. The absolute lesion signals appear to be slightly greater in the prone orientation, where breast tissue is more spread out and is pendant away from the torso, but also have higher variability. To some extent, prone PET images present better image quality than supine PET images in terms of SNR and contrast uniformity. However, the uniformity of the signal intensity is worse in prone orientation, accompanied by several unexpected image artifacts. Changes in local contrast are equivocal in the two different orientations. From the paired t-test results, there are no significant differences between prone and supine in terms of local contrast.

The prone setup makes it easier to locate the lesions in the breast phantoms in the cases of this study, but because the breast phantom does not behave exactly like a human breast and the lesions inside the phantom may not move as in real breasts from supine to prone orientation, it may not be the same for a real patient. As future work, either more realistic phantom studies and/or real patients with known lesions should be evaluated in order to investigate some of these discrepancies.

**Appendix 1: BI-RADS Assessment Categories and Management Recommendations.**

<b>Assessment</b>		<b>Likelihood of Cancer</b>	<b>Management</b>
Category 0: Incomplete-Need Additional Imaging Evaluation and/or Prior Mammograms for Comparison		N/A	Recall for additional imaging and/or comparison with prior examinations.
Category 1: Negative		Essentially 0% likelihood of malignancy	Routine mammography screening.
Category 2: Benign		Essentially 0% likelihood of malignancy	Routine mammography screening.
Category 3: Probably Benign		0% ~ 2% likelihood of malignancy	Short-interval (6-month) follow-up or continued surveillance mammography.
Category 4: Suspicious	Category 4A: Low suspicion for malignancy	2% ~10% likelihood of malignancy	Tissue diagnosis.
	Category 4B: Moderate suspicion for malignancy	10% ~ 50% likelihood of malignancy	
	Category 4C: High suspicion for malignancy	50% ~ 95% likelihood of malignancy	
Category 5: Highly Suggestive of Malignancy		≥ 95% likelihood of malignancy	Tissue diagnosis.
Category 6: Known Biopsy-Proven Malignancy		N/A	Surgical excision when clinically appropriate.

**Appendix 2: Review – Breast Phantoms in Different Imaging Modalities.**

	Reference number	[11]	[40]	[12]	[13]	[14]	[15]	[16]	[17]	[18]	[19]	[20]	[21]	[22]	[23]	[24]	[25]	[26]	[41]	[42]	[43]	[27]	[44]	[30]	[45]
<b>Imaging Modality Applied</b>	MRI			√					√				√		√					√			N/A		√
	Ultrasound				√						√	√				√	√	√			√		N/A		
	X-ray	√	√			√	√				√		√	√					√			√	N/A		√
	Nuclear Medicine							√		√	√		√										N/A	√	
	Reference number	[11]	[40]	[12]	[13]	[14]	[15]	[16]	[17]	[18]	[19]	[20]	[21]	[22]	[23]	[24]	[25]	[26]	[41]	[42]	[43]	[27]	[44]	[30]	[45]
<b>Materials Involved</b>	Gelatin	N/A	N/A					√	N/A	N/A	√		√	N/A	√	√	√					N/A	N/A	N/A	
	Agar	N/A	N/A						N/A	N/A	√		√	N/A		√	√	√					N/A	N/A	N/A
	Resin	N/A	N/A		√	√	√		N/A	N/A				N/A									N/A	N/A	N/A
	Lard	N/A	N/A	√		√			N/A	N/A				N/A									N/A	N/A	√
	Glycerin	N/A	N/A						N/A	N/A		√		N/A	√								N/A	N/A	N/A
	Egg White	N/A	N/A	√		√			N/A	N/A				N/A									N/A	N/A	√
	Paraffin Wax	N/A	N/A						N/A	N/A				N/A					√				N/A	N/A	N/A
	Beeswax	N/A	N/A			√			N/A	N/A				N/A									N/A	N/A	N/A
	Chemical Gel	N/A	N/A							N/A	N/A				N/A						√	√	N/A	N/A	N/A
	Graphite Powder	N/A	N/A							N/A	N/A				N/A	√	√					√	N/A	N/A	N/A
	Silicone	N/A	N/A							N/A	N/A				N/A			√					N/A	N/A	N/A
	Latex	N/A	N/A					√		N/A	N/A				N/A								N/A	N/A	N/A

**Appendix 2: Review – Breast Phantoms in Different Imaging Modalities (continued).**

	<b>Reference number</b>	[11]	[40]	[12]	[13]	[14]	[15]	[16]	[17]	[18]	[19]	[20]	[21]	[22]	[23]	[24]	[25]	[26]	[41]	[42]	[43]	[27]	[44]	[30]	[45]
<b>Fabrication Technique</b>	Manually Casted			√			√	√			√		√	√				√		√				N/A	√
	Prototyping	N/A	√		√				N/A	N/A					N/A	N/A	N/A		N/A		N/A		N/A	N/A	
	Inkjet Printing	A							A	A					A	A	A		A		A	√	A		
	3D Printing					√						√													
	<b>Reference number</b>	[11]	[40]	[12]	[13]	[14]	[15]	[16]	[17]	[18]	[19]	[20]	[21]	[22]	[23]	[24]	[25]	[26]	[41]	[42]	[43]	[27]	[44]	[30]	[45]
<b>Feature of the phantom</b>	Anthropomorphic			√	√	√														√					√
	Compressible or Compressed in shape	N/A	N/A		√	√	√	√				√	√		N/A	N/A	N/A		N/A		N/A	√	N/A		√
	Uncompressible or rigid			√					√	√	√			√				√		√				√	
	Inner Lesion						√	√		√	√							√							
	Fillable			√		√		√	√	√	√			√											√

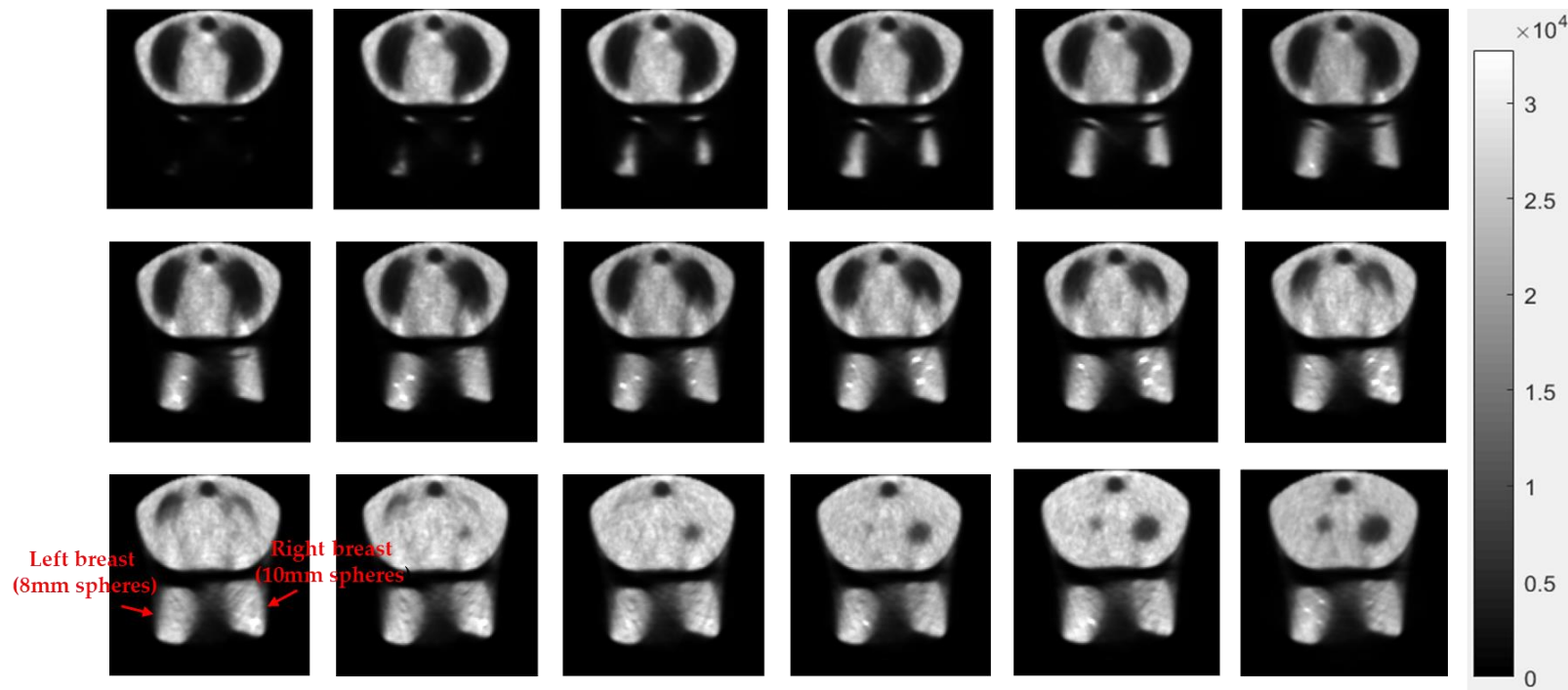
### Appendix 3: Slime material tests.

Experiment number	Volume (mL)		Concentration of borax solution (g/L)	Temperature (°C)	Volume of upper solution left (mL)	Time of formation (min)	Other conditions	Comments
	Borax solution	Glue						
1	50	50	6	23	20	4	/	elastic, stretchy, shapeable, and viscous
2	50	100	6	23	/	/	/	failed
3	100	50	6	23	70	4	red pigment added into the borax solution	elastic, stretchy, shapeable, viscous, plus uniform distribution of coloring
4	50	50	6	23	20	4	blue pigment added into the glue	elastic, stretchy, shapeable, viscous, plus uniform distribution of coloring
5	50	50	10	50	20	2	microwave heat the saturated solution with borax sediment about 2min	a little hard, less elastic, less stretchy, faster formation
6	50	50	3	23	20	4	dilute the saturated borax solution by half under room temperature	elastic, stretchy, shapeable, and viscous

**Appendix 4: Gelatin material test.**

Experiment number	Volume of water (mL)	Amount of Gelatin		Temperature (°C)	Time of formation (h)	Comments
		Weight (g)	Percentage (%)			
1	200	2	1%	70	/	Failed because of not enough gelatin
2	200	5	2.5%	70	~1	Very soft and elastic jelly, not malleable
3	200	10	5%	70	~1	Relatively soft and elastic-rubber texture, not malleable

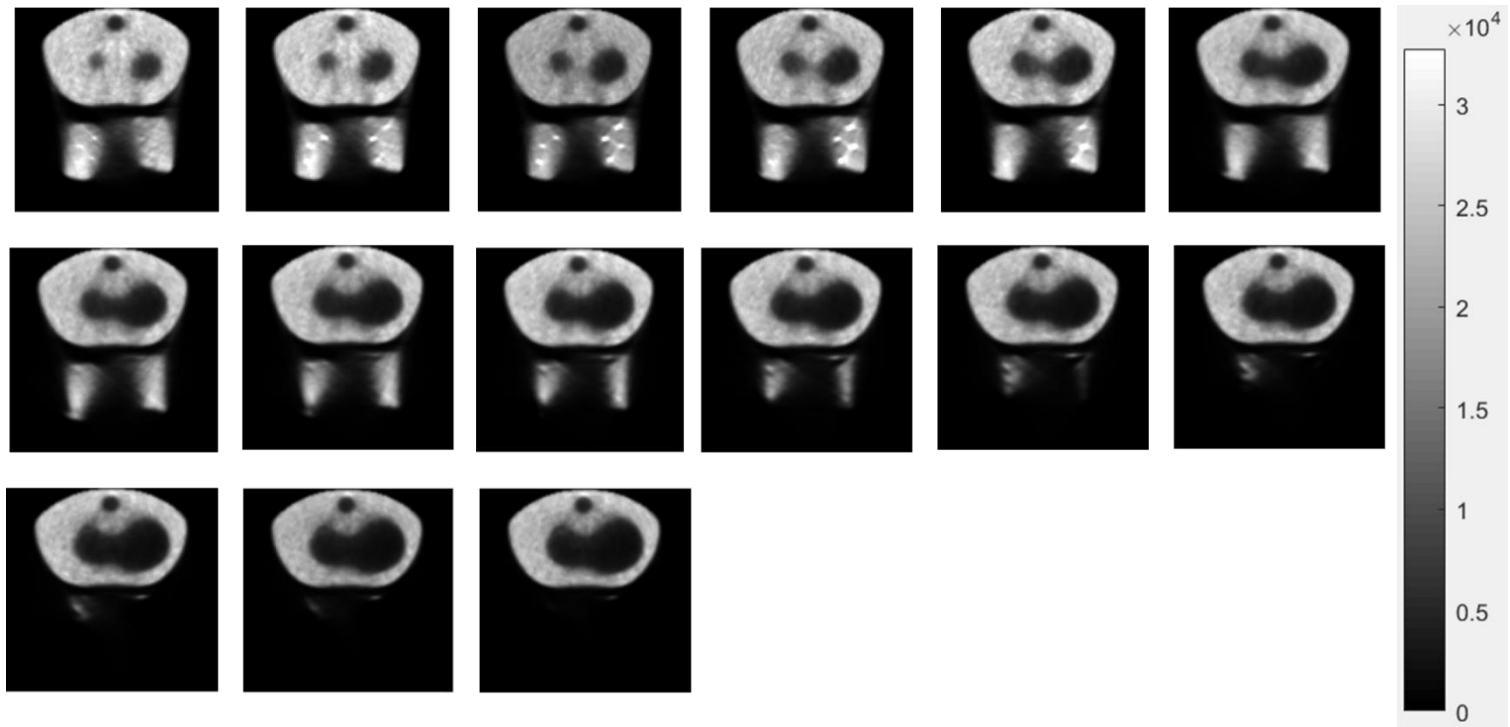
Appendix 5: Matrix of images (PET, prone, 420 sec reconstruction)<sup>1</sup>



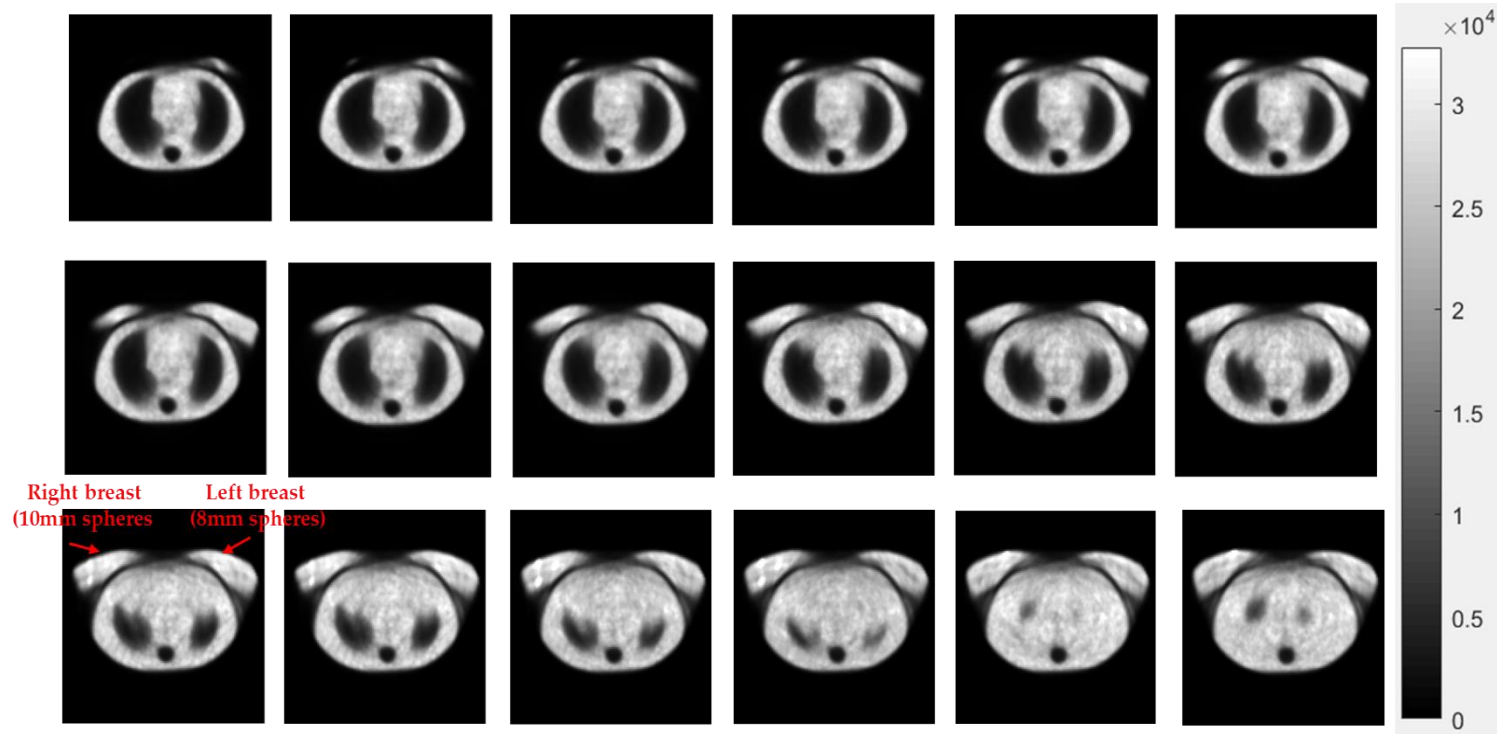
<sup>1</sup> Reconstructed images start from most superior transaxial slice in the upper left and progress towards most inferior slice (near liver) in the lower right (image slices continue on the next page). Note that the left and right breasts are labeled in the lower-left image; the same orientation applies to the corresponding prone CT images in Appendix 7. Image matrix size:  $128 \times 128$ ; Pixel size:  $3.9 \times 3.9 \text{ mm}^2$ ; Slice thickness: 3.26 mm; FOV:  $50 \times 50 \text{ cm}^2$ ; The gray scale of all the PET images is normalized to the global maximum as shown in the color bar (the number represents pixel values in Bq/mL units).

**Appendix 5 (continued): Matrix of images (PET, prone, 420 s reconstruction)**

(Image parameters are identical to those on previous page of related data.)



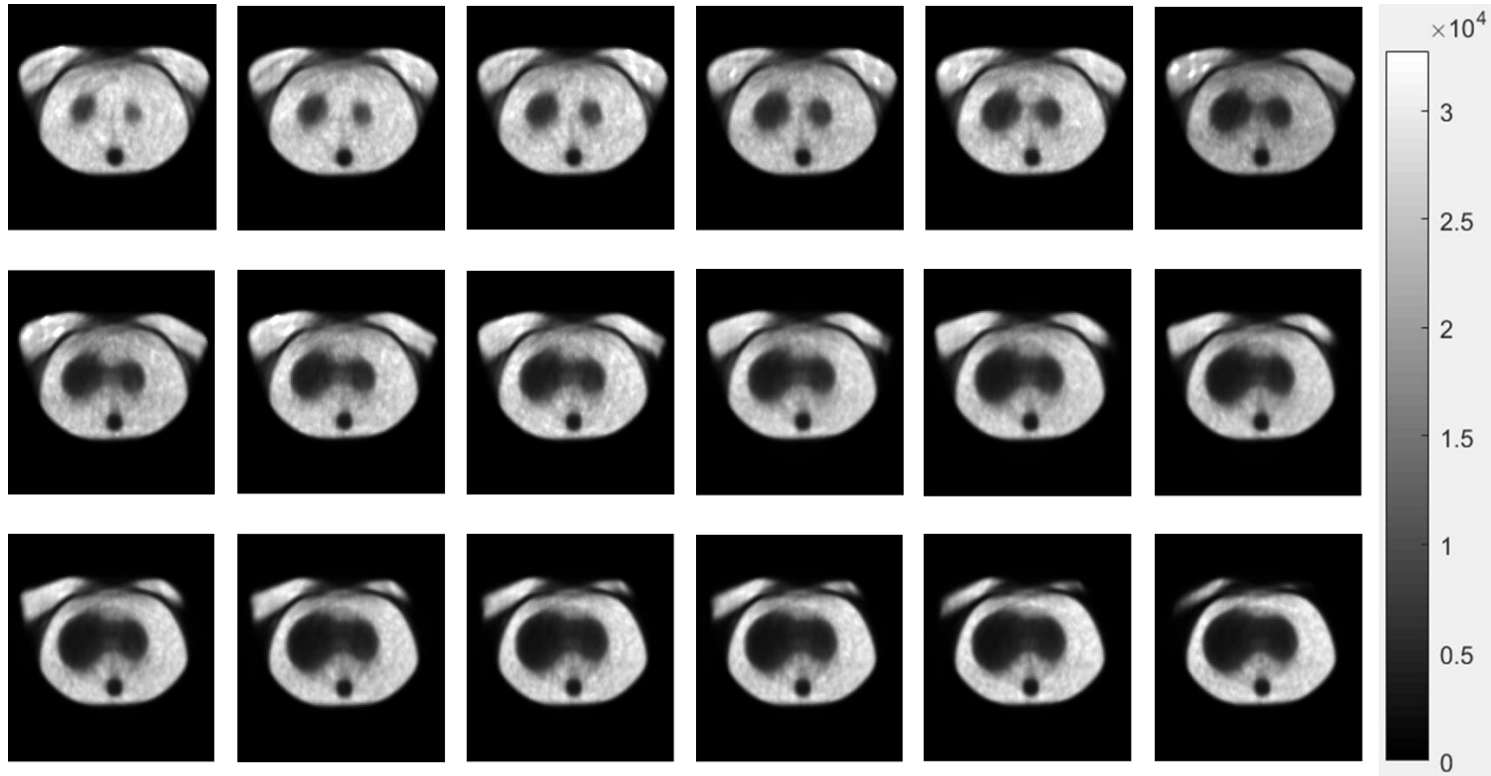
Appendix 6: Matrix of images (PET, supine, 513 sec reconstruction)<sup>1</sup>



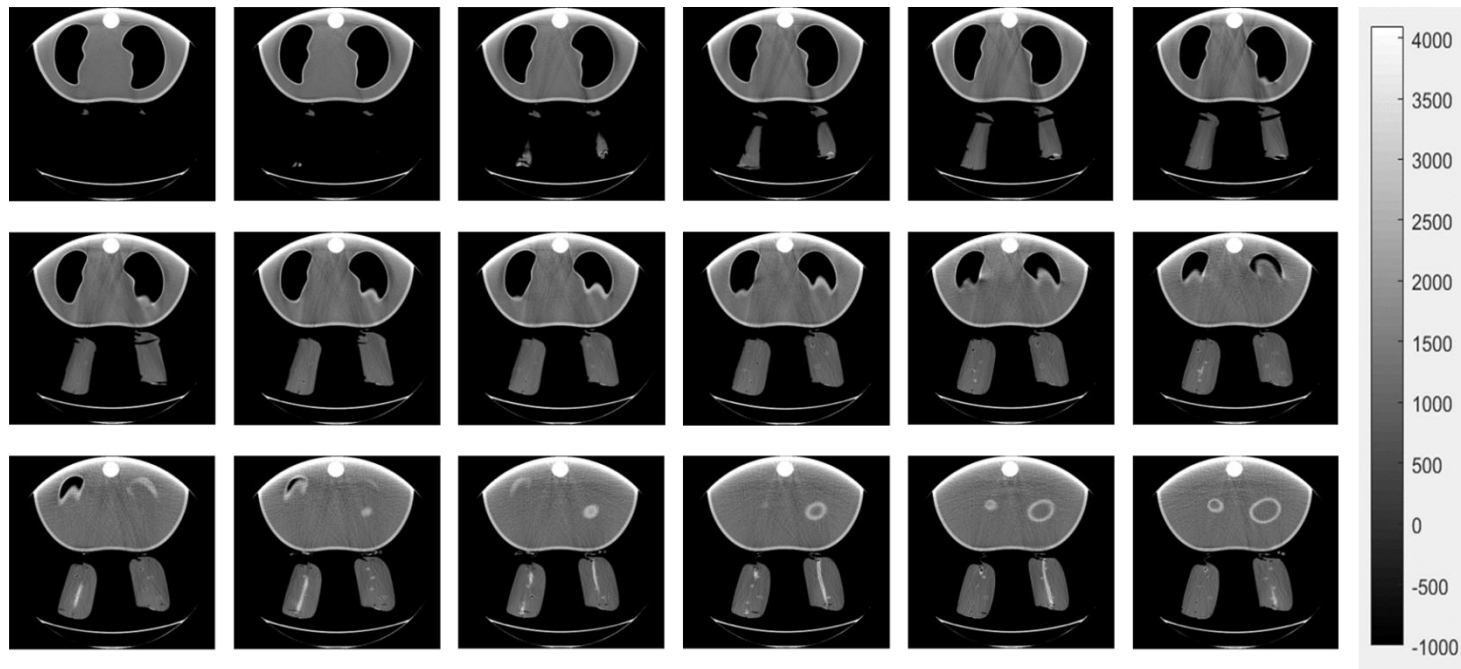
<sup>1</sup> Reconstructed images start from most superior transaxial slice in the upper left and progress towards most inferior slice (near liver) in the lower right (image slices continue on the next page). Note that the left and right breasts are labeled in the lower-left image, and the same orientation applies to the corresponding prone CT images in Appendix 8. Image matrix size:  $128 \times 128$ ; Pixel size:  $3.9 \times 3.9 \text{ mm}^2$ ; Slice thickness: 3.26 mm; FOV:  $50 \times 50 \text{ cm}^2$ ; The gray scale of all the PET images is normalized to the global maximum as shown in the color bar (the number represents pixel values in Bq/mL units).

Appendix 6 (continued): Matrix of images (PET, supine, 513 sec acquisition)

(Image parameters are identical to those on previous page of related data.)



### Appendix 7: Matrix of images (CT, prone)<sup>1</sup>

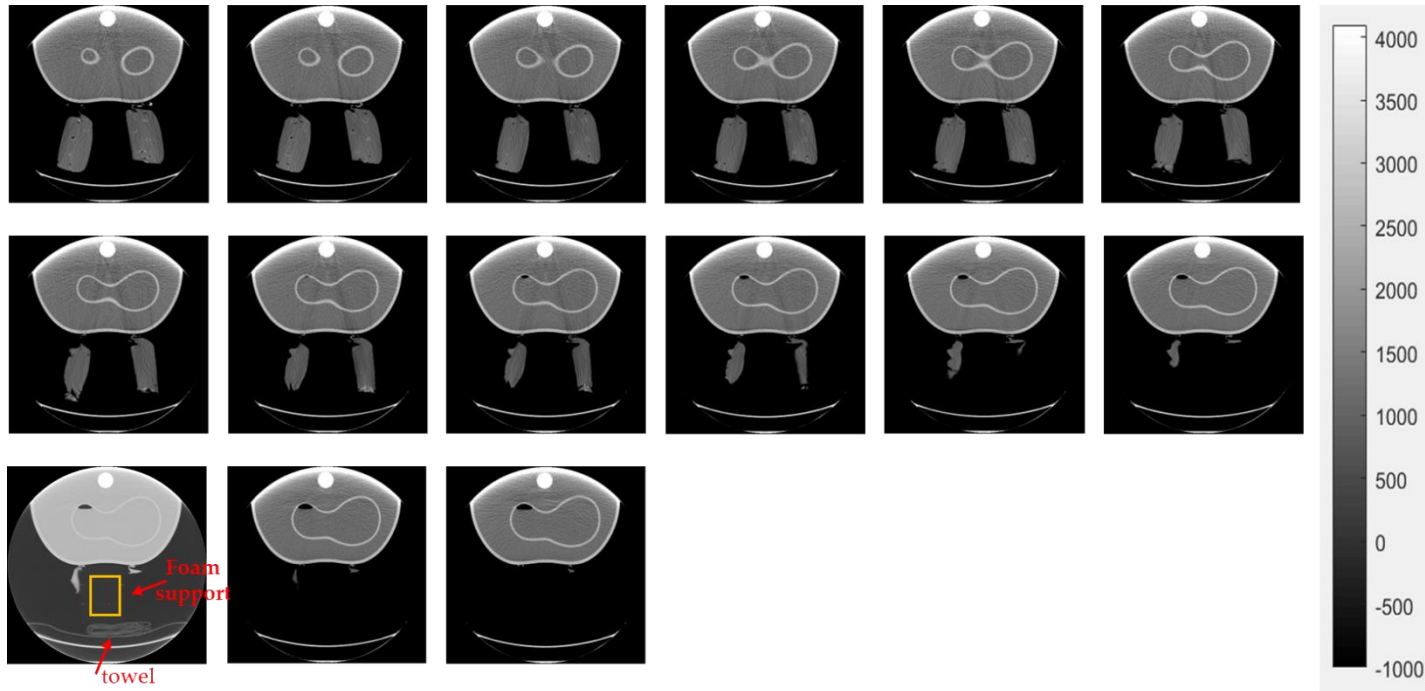


75

<sup>1</sup> Images start from most superior transaxial slice in the upper left and progress towards most inferior slice (near liver) in the lower right (image slices continue on the next page). The gray scale of all the CT images are normalized to the same global maximum as shown in the color bar (the number represents CT number). Matrix size:  $512 \times 512$ ; Pixel size:  $0.9766 \times 0.9766 \text{ mm}^2$ ; Slice thickness:  $3.26 \text{ mm}$ ; FOV:  $50 \times 50 \text{ cm}^2$ .

### Appendix 7 (continued): Matrix of images (CT, prone)<sup>1</sup>

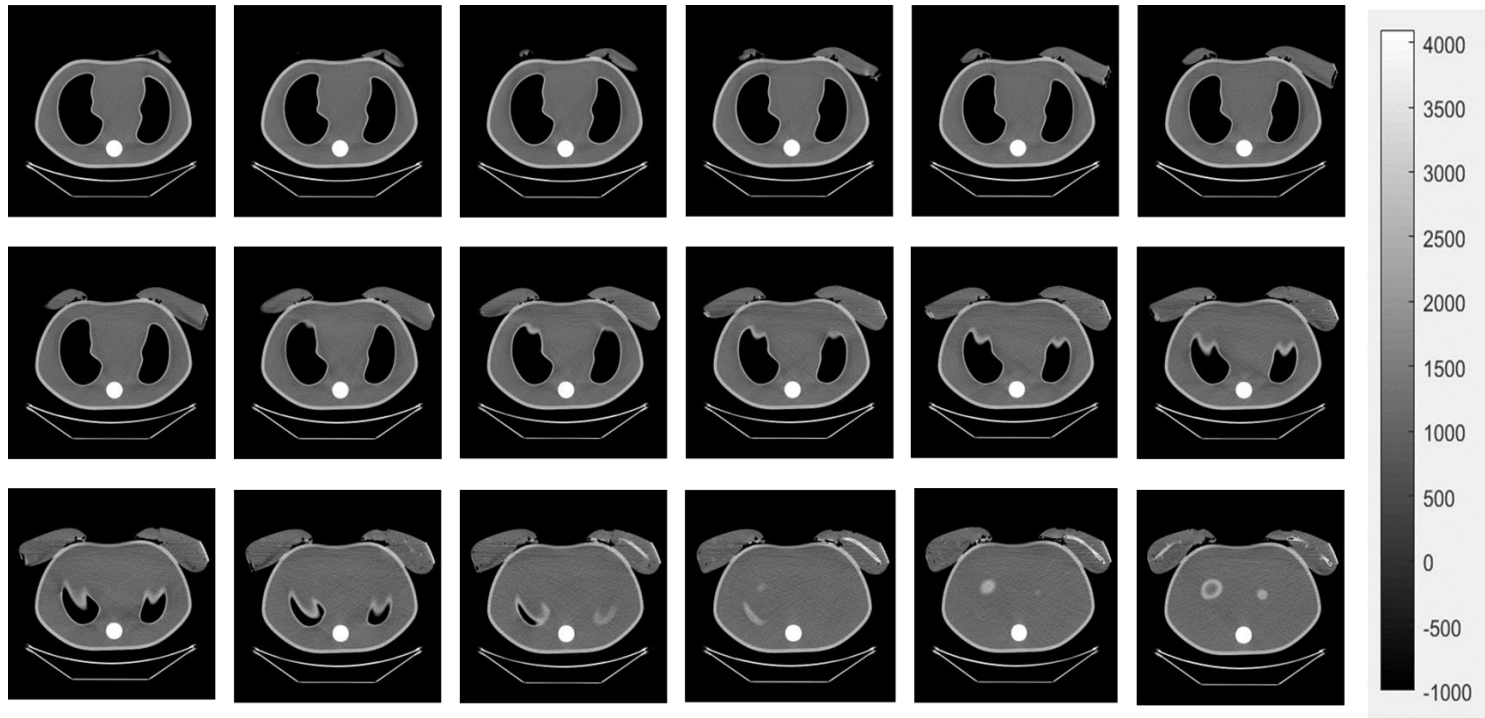
(Image parameters are identical to those on previous page of related data.)



---

<sup>1</sup> Note that the window level is adjusted for the lower-left image so that the foam support can be somewhat better visualized in the image. Due to the curvature of the PET/CT bed, a towel was placed beneath the torso support for stabilization. The average value of the yellow rectangular ROI is -966.7 which is close to the Hounsfield unit of air (-1000). Therefore, the torso support has little attenuation or scatter effect to the photons.

### Appendix 8: Matrix of images (CT, supine)<sup>1</sup>



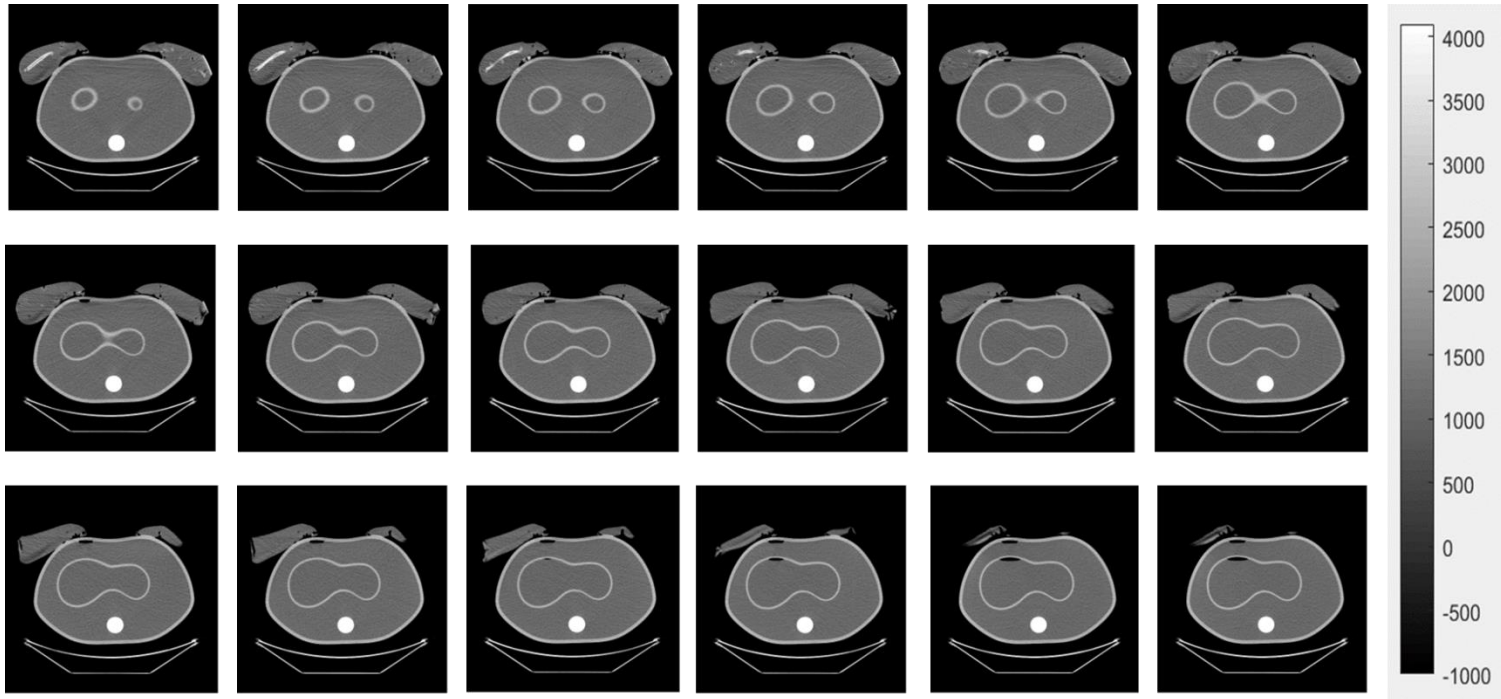
77

---

<sup>1</sup> Images start from most superior transaxial slice in the upper left and progress towards most inferior slice (near liver) in the lower right (image slices continue on the next page). The gray scale of all the CT images are normalized to the same global maximum as shown in the color bar (the number represents CT number). Matrix size:  $512 \times 512$ ; Pixel size:  $0.9766 \times 0.9766 \text{ mm}^2$ ; Slice thickness: 3.26 mm; FOV:  $50 \times 50 \text{ cm}^2$ .

### Appendix 8 (continued): Matrix of images (CT, supine)

(Image parameters are identical to those on previous page of related data.)



## Appendix 9: MRI experiment

As additional experience and to gather more information, an MR scan was performed a few days later after radioactive decay, as a comparison to the prone PET/CT scans. A *Siemens Skyra 3T* MR scanner was used. Ideally, the same phantoms in the same configurations should be used for all the experiments, however, some adjustments were made to the breast phantoms and they were re-taped onto the torso phantom for the MR experiment. Therefore, note that there are some differences in the phantom setups in the PET/CT measurements and MR experiment, and it may influence the final results.

The breast+torso phantom was placed on the *In vivo Sentinelle* MR-breast coil (Figure 21) in the prone orientation. Since the  
79 breasts were disassembled from the torso phantom after the PET/CT scans were completed, some repositioning was carefully accomplished on the phantoms when reassembling them for the MR scan. Specifically, the breast phantoms were removed and emptied of their contents (after  $^{18}\text{F}$  radioactive decay) after the PET/CT scans, and thus needed to be refilled with the fluid-containing lesions and a saline background volume. In addition, the phantoms were removed from the radiolucent foam support and repositioned on the MR-breast coil including patient pads not previously utilized during the PET/CT scans. Therefore, the phantom setup in the MR scanner should be similar but not exactly the same as the prone PET/CT setup. Several foam pieces were padded around the phantom for additional immobilization, and the two pendent saline bags were fitted into the hollow space of

the coil (not visible in Figure 21). Short T<sub>1</sub> inverse recovery (STIR) technique was used to acquire the MR images. The complete parameter settings for the MR experiment is listed in Table 17. The acquired MR images are also listed in matrix as shown in Figure 22 and Figure 23.

**Table 17: MR scan parameters**

Experiment	Technique	Echo time (ms)	Repetition time (ms)	FOV (cm <sup>2</sup> )	Scan range (cm)	Slice thickness (mm)	Number of slices	Pixel size
MR	STIR	2.46	5.43	50 × 50	26	3.8	70	0.9766 × 0.9766



**Figure 21: Phantom setup for the prone-only MR scan using the *Sentinelle* breast coil and *Siemens Skyra* scanner.**

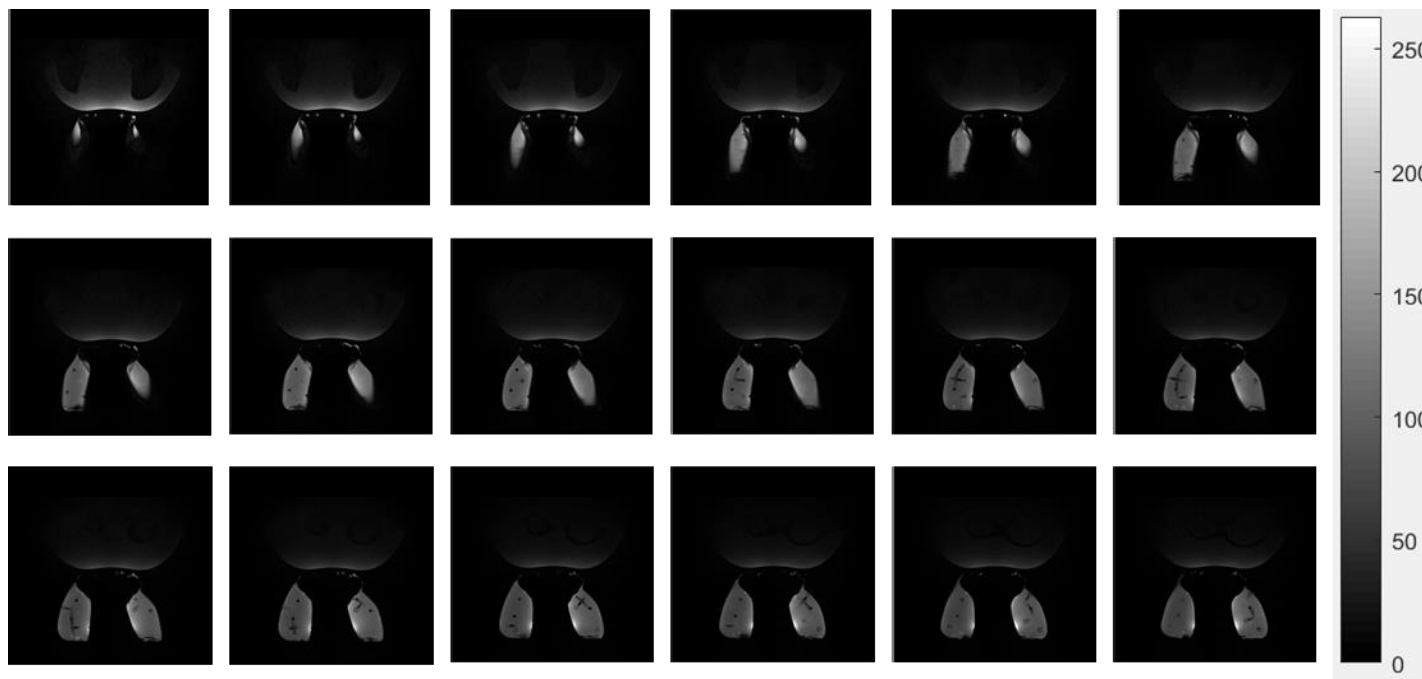


Figure 22: Matrix of images (MR, prone, STIR technique)<sup>1</sup>

---

<sup>1</sup> Images start from most superior transaxial slice in the upper left and progress towards most inferior slice (near liver) in the lower right (image slices continue on the next page). [The gray scale of all the MR images are normalized to the same global maximum as shown in the color bar (the number represents MR pixel value). Matrix size:  $512 \times 512$ ; Pixel size:  $0.9766 \times 0.9766 \text{ mm}^2$ ; Slice thickness: 3.8 mm; FOV:  $50 \times 50 \text{ cm}^2$ .

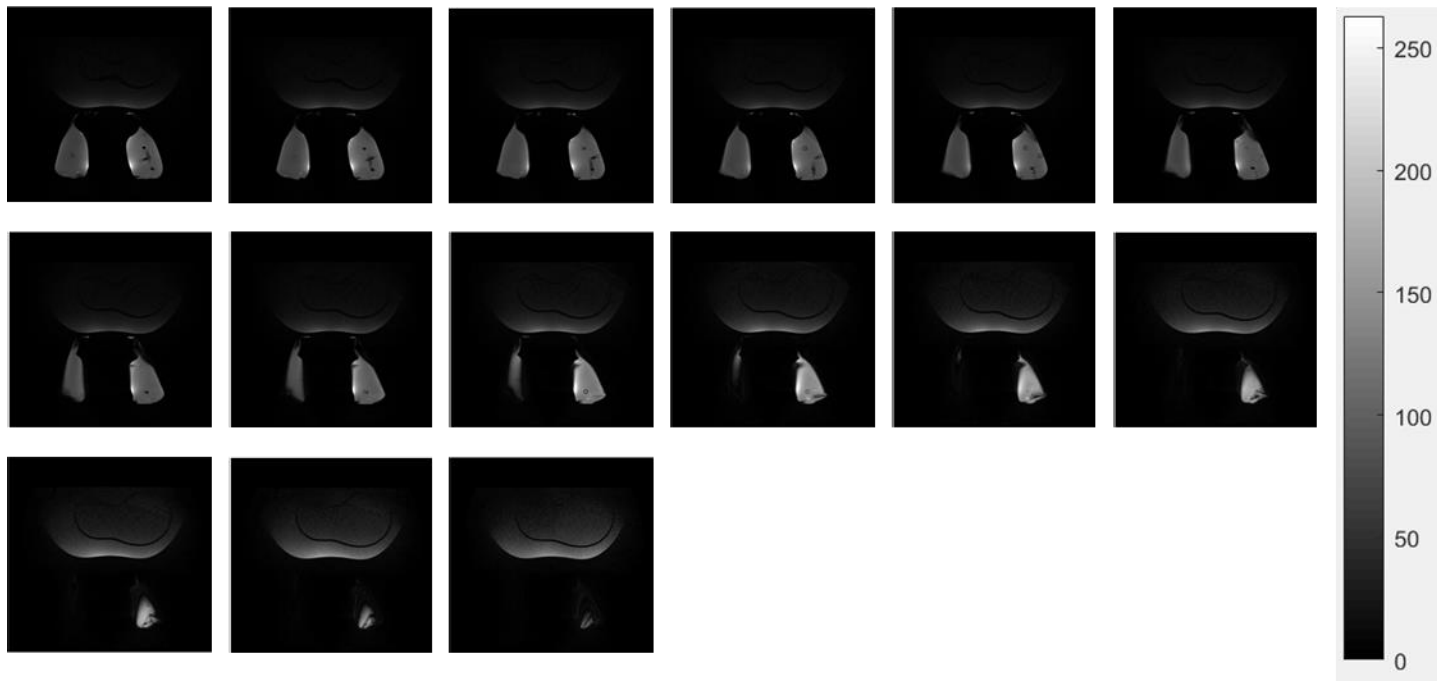


Figure 23 (continued): Matrix of images (MR, prone, STIR technique)

## References

- [1] M. M. Koo, C. von Wagner, G. A. Abel, S. McPhail, G. P. Rubin, and G. Lyratzopoulos, "Typical and atypical presenting symptoms of breast cancer and their associations with diagnostic intervals: Evidence from a national audit of cancer diagnosis," *Cancer Epidemiology*, vol. 48, pp. 140–146, Jun. 2017.
- [2] A. R. Kherlopian et al., "A review of imaging techniques for systems biology," *BMC Systems Biology*, vol. 2, no. 1, p. 74, 2008.
- [3] R. R. Devi and G. S. Anandhamala, "Recent Trends in Medical Imaging Modalities and Challenges for Diagnosing Breast Cancer," *Biomedical and Pharmacology Journal*, vol. 11, no. 3, pp. 1649–1658, Sep. 2018.
- [4] A. Bleyer and H. G. Welch, "Effect of Three Decades of Screening Mammography on Breast-Cancer Incidence," *New England Journal of Medicine*, vol. 367, no. 21, pp. 1998–2005, Nov. 2012.
- [5] S. Amano, T. Inoue, K. Tomiyoshi, T. Ando, and K. Endo, "In Vivo Comparison of PET and SPECT Radiopharmaceuticals in Detecting Breast Cancer," *Journal of Nuclear Medicine*, vol. 39, No. 8, pp. 1424–1427, Aug. 1998.
- [6] B. B. Koolen, W. V. Vogel, M. J. T. F. D. Vrancken Peeters, C. E. Loo, E. J. T. Rutgers, and R. A. Valdés Olmos, "Molecular Imaging in Breast Cancer: From Whole-Body PET/CT to Dedicated Breast PET," *Journal of Oncology*, vol. 2012, pp. 1–8, 2012.
- [7] L. MacDonald, J. Edwards, T. Lewellen, D. Haseley, J. Rogers, and P. Kinahan, "Clinical imaging characteristics of the positron emission mammography camera: PEM Flex Solo II," *Journal of Nuclear Medicine*, vol. 50, no. 10, pp. 1666–1675, 2009.
- [8] Y. Wu, S. L. Bowen, K. Yang et al., "PET characteristics of a dedicated breast PET/CT scanner prototype," *Physics in Medicine and Biology*, vol. 54, no. 13, pp. 4273–4287, 2009.

- [9] A. Soriano, A. Gonzalez, A. Orero et al., "Attenuation correction without transmission scan for the MAMMI breast PET," *Nuclear Instruments and Methods in Physics Research A*, vol.648, supplement 1, pp. S75–S78, 2011.
- [10] M. Z. Unlu et al., "Computerized method for nonrigid MR-to-PET breast-image registration," *Computers in Biology and Medicine*, vol. 40, no. 1, pp. 37–53, Jan. 2010
- [11] R. A. Geise, A. Palchevsky (1996). "Composition of Mammographic Phantom Materials." *Medical Physics* 198(2): 347-350.
- [12] M. Freed, J. A. Zwart, J. T. Loud, R. H. Khouli, K. J. Myers, M. H. Greene, J. H. Duyn, A. Badano (2011). "An Anthropomorphic Phantom For Quantitative Evaluation Of Breast MRI." *Medical Physics* 38: 743-754.
- [13] A. K. Carton, P. Bakic, C. Ullberg, H. Derand, A. D. A. Maidment (2011). "Development Of A Physical 3D Anthropomorphic Breast Phantom." *Medical Physics* 38(2): 891-897.
- [14] N. Kiarashi, A. C. Nolte, G. M. Sturgeon, W. P. Segars, S. V. Ghate, L. W. Nolte, E. Samei, J. Y. Lo (2015). "Development Of Realistic Physical Breast Phantoms Matched To Virtual Breast Phantoms Based On Human Subject Data." *Medical Physics* 42: 4116-4127.
- [15] J. M. Arvelos, M. B. Flores, F. Amaral, M. Chevalier, A. P. Mourão (2017). "Development of Breast Phantom For Quality Assessment of Mamographic Images." 2017 International Nuclear Atlantic Conference. Belo Horizonte, MG, Brazil (978-85-99141-07-6): 1-8.
- [16] D. Kieper et al., "Optimization of breast imaging procedure with dedicated compact gamma cameras," *Nuclear Instruments and Methods in Physics Research Section A*, vol. 497, no. 1, pp. 168–173, Jan. 2003.
- [17] B. Tuong, I. Gardiner (2013). "Development of a Novel Breast MRI Phantom for Quality Control." *American Journal of Roentgenology* 201: 511-516.

- [18] M. P. Tornai, R. L. Mckinley, C. N. Brzymialkiewicz, S. J. Cutler, D. J. Crotty (2005). "Anthropomorphic Breast Phantoms for Preclinical Evaluation with Transmission or Emission Imaging." *SPIE Physiology, Function, and Structure from Medical Images* 5746(2): 825-834.
- [19] J. Dang et al., "Development of an Anthropomorphic Breast Phantom for Combined PET, B-Mode Ultrasound and Elastographic Imaging," *IEEE Transactions on Nuclear Science*, vol. 58, no. 3, pp. 660–667, Jun. 2011.
- [20] T. Rydholm, A. Fager, M. Persson, S. D. Geimer, P. M. Meaney (2018). "Effects of the Plastic of the Realistic GeePS-L2S-Breast Phantom." *Diagnostics*: vol. 61, 1-18.
- [21] J. S. Huber, Q. Peng, W. W. Moses (2009). "Multi-Modality Phantom Development." *IEEE Transactions on Nuclear Science* 56(5): 2722-2727.
- [22] J. P. Shah, S. D. Mann, M. P. Tornai (2017). "Characterization of X-ray Scattering For Various Phantoms and Clinical Geometries Using Breast CT on a Dedicated Hybrid System." *Journal of X-ray Science and Technology* 25: 373-389.
- [23] E. L. Madsen, G. D. Fullerton (1982). "Prospective Tissue-Mimicking Materials For Use in NMR Imaging Phantoms." *Magnetic Resonance Imaging* 1(3): 135-142.
- [24] C. L. Korte, E. I. Cespedes, A. F. W. Steen, B. Norder, K. Tenijenhuis (1997). "Elastic and Acoustic Properties of Vessel Mimicking Material for Elasticity Imaging." *Ultrasonic Imaging* 19: 112-127.
- [25] H. M. Ismail, C. G. Pretty, M. K. Signal, M. Haggars, C. Zhou, and J. G. Chase, "Mechanical behaviour of tissue mimicking breast phantom materials," *Biomedical Physics & Engineering Express*, vol. 3, no. 4, p. 045010, Jul. 2017.
- [26] S. P. Foroozandehasl, M. S. Jaafar (2011). "A Study on Breast Phantom Using Ultrasound Imaging Systems." *IEEE (978-1-61284-896-9)*: 1-4.
- [27] L. C. Ikejimba, C. G. Graff, S. Rosenthal, A. Badal, B. Ghamraoui, J. Y. Lo, S. J. Glick, (2017). "A Novel Physical Anthropomorphic Breast Phantom For 2D And 3D X-Ray

Imaging." *Medical Physics* 44 (2): 4007-4016.

- [28] S. Sha, "Applicational Breast Phantoms in Different Imaging Modalities—A Literature Review" (2018), Duke University, Durham, USA, unpublished material.
- [29] H. Grigg and G. Newman, "Bolus over – Super Stuff ®," p. 2.
- [30] J. M. Williams et al., "Comparison of prone versus supine 18F-FDG-PET of locally advanced breast cancer: Phantom and preliminary clinical studies: Prone vs supine FDG PET of breast cancer," *Medical Physics*, vol. 42, no. 7, pp. 3801–3813, Jun. 2015.
- [31] S. J. Cutler, D. J. Crotty, M. P. Tornai. "Dynamic Laser-Guided Contouring for Dedicated Emission Mammotomography." 2008 IEEE Conference Record NSS/MIC, 4789-4793.
- [32] A. Taha and A. Hanbury, "Metrics for evaluating 3D medical image segmentation: analysis, selection, and tool," *BMC Medical Imaging*, vol. 15, no. 1, pp. 15-29, Dec. 2015.
- [33] R. Shier, "Paired t-test" 2004, Mathematics Learning Support Center, pp. 1-3.
- [34] M. Soret, S. L. Bacjarach, I. Buvat. "Partial-Volume Effect in PET Tumor Imaging," *Journal of Nuclear Medicine*, vol. 48 no. 6, pp. 932-945, June 2007.
- [35] W. W. Moses, "Fundamental limits of spatial resolution in PET," *Nuclear Instruments and Methods in Physics Research Section A*, vol. 648, pp. S236–S240, Aug. 2011.
- [36] R. L. Wahl, H. Jacene, Y. Kasamon, and M. A. Lodge, "From RECIST to PERCIST: Evolving Considerations for PET Response Criteria in Solid Tumors," *Journal of Nuclear Medicine*, vol. 50, no. Suppl\_1, pp. 122S-150S, May 2009.

- [37] Z. Gong and M. B. Williams, "Comparison of Breast Specific Gamma Imaging and Molecular Breast Tomosynthesis in Breast Cancer detection: Evaluation in Phantoms," *Medical Physics*, vol. 42, no. 7, pp. 4250-4259, June 2015.
- [38] N. Avril et. al., "Breast Imaging with Fluorine-18-FDG PET: Quantitative Image Analysis," *Journal of Nuclear Medicine*, vol.38, no.8, pp. 1186-1191, Aug. 1997.
- [39] S. J. Lee, Y. Y. Choi, C. Kim, and M. S. Chung, "Correlations Between Tumor to Background Ratio on Breast-Specific Gamma Imaging and Prognostic Factors in Breast Cancer," *Journal of Korean Medical Science*, vol. 32, pp. 1031-1037, Mar. 2017.
- [40] P. C. Johns, M. J. Yaffe (1987). "X-ray Characterization of Normal and Neoplastic Breast Tissues." *Physics in Medicine and Biology* 32: 675-695.
- [41] S. Cubukcu, H. Yücel (2015). "Development of Breast Tissue Equivalent Phantom Made From Paraffin With Some Additives And Its Characterization By Using X-Ray Spectroscopy". *European Society of Radiology*: 1-12.
- [42] G. P. Mazzara, R. W. Briggs, Z. Wu, B. G. Steinbach (1996). "Use Of A Modified Polysaccharide Gel In Developing A Realistic Breast Phantom For MRI." *Magnetic Resonance Imaging* 14: 639-649.
- [43] E. L. Madsen, J. A. Zagzebski, R. A. Banjavie, R. E. Jutila (1978). "Tissue Mimicking Materials for Ultrasound Phantoms." *Medical Physics* 5(5): 391-395.
- [44] J. Maublant, M. Latour, D. Mestas, A. Clemenson et al (1996). "Technetium-99m-Sestamibi Uptake in Breast Tumor and Associated Lymph Nodes." *Journal of Nuclear Medicine* 37(6): 922-925.
- [45] M. Freed, A. Badal, R. J. Jennings, H. Heras, K. J. Myers, A. Badano (2011). "X-Ray Properties Of An Anthropomorphic Breast Phantom For MRI And X-Ray Imaging." *Physics in Medicine and Biology* 56: 3513-3533.